To the Graduate Council:

I am submitting herewith a thesis written by Brent Ellis entitled “Predictive Models of an Electro-mechanical Driving System for Failure Testing of Stain Gauges.” I have examined the final electronic copy of this thesis for form and content and recommend that it be accepted in partial fulfillment of the requirements for the degree of Master of Science, with a major in Electrical Engineering.

_____

Dr. L. Montgomery Smith, Major Professor

We have read this thesis

and recommend its acceptance:

Dr. Bruce Bomar_____

Dr. Roy Schulz_____

Accepted for the Council:

Carolyn R. Hodges_____

Vice Provost and Dean of the
Graduate School

(Original signatures are on file with official student records)

PREDICTIVE MODELS OF AN ELECTRO-MECHANICAL DRIVING SYSTEM FOR FAILURE TESTING OF STRAIN GAUGES

A Thesis
Presented for the
Masters of Science
Degree
The University of Tennessee Space Institute

Brent Ellis
August 2007

DEDICATION

To Ashley, for her love and support

ACKNOWLEDGEMENTS

I would first and foremost like to thank my wife, Ashley. Her constant support throughout the completion of this degree has been my driving force, and in return she has always had my constant love and support throughout her graduate work. Spending so much time apart during the completion of this work has given me a better appreciation of what it means to be together.

I would like to thank my family for rearing me with the desire to succeed and learn. Without their support and guidance I could have never succeeded in my graduate studies. I would also like to thank all of my friends for the support and good times throughout my college experience.

I would like to thank my advisor, Dr. L. Montgomery Smith, for his guidance and constructive criticism during the completion of this thesis. I also thoroughly enjoyed each class he taught during my graduate experience at UTSI.

I would like to thank the other members of my committee, Dr. Bruce Bomar and Dr. Roy J. Schulz for their feedback and contributions to this paper. I would also like to thank the Department of Electrical Engineering at Christian Brothers University and The University of Tennessee Space Institute for providing me with the best education I could receive.

ABSTRACT

Strain gauges are bonded at high stress locations on the surface of critical structural components such as turbine blades to measure fatigue characteristics and detect early warning signs of high cycle fatigue. However, strain gauges do not always report expected measurements. The usual response by maintenance technicians to these failing signals is to investigate the component for weakness, check the placement of the gauges on the component, or examine the instrumentation for failure or damage. However, little research has been conducted to show when the failing signals are the fault of the strain gauge. Such failure modes of strain gauges include improper gauge installation, over-straining, operating outside the temperature limits, physical damage and environmental wear, and improper gauge selection. Failure Modes and Effects Analysis, FMEA, is a methodology for monitoring failure modes and their potential effects, causes, and solutions. This research consisted of the introductory steps in developing and analyzing a laboratory setup for FMEA strain gauge testing and analysis. The primary goal of this research was to develop predictive models for strain gauge responses under controlled laboratory conditions. A testing station was developed that generated a mechanical motion on a beam, subjecting strain gauges to a sinusoidally-varying strain. Predictive models of the testing station were developed and experimentally analyzed. Models were also developed for two particular failure modes, debonding and wire lead termination, and experimental analysis was conducted. In general, the models adequately describe the operation of a strain gauge operating under normal conditions and in the studied failure mode. Predicted and experimental data are presented that show the characteristic signals in terms of time domain, histogram, and frequency domain analysis.

TABLE OF CONTENTS

CHAPTER I **1**
INTRODUCTION AND MOTIVATION **1**
1.1. Introduction 1
1.2. Objectives 3
1.3. Outline 5
CHAPTER II **7**
STRAIN GAUGE TECHNOLOGY **7**
2.1. Mechanical strain 7
2.2. The resistance strain gauge 8
2.3. Fundamental operation of a strain gauge 9
2.4. The Wheatstone bridge 11
2.5. The Vishay® EA-06-062AP-120 120Ω strain gauge 12
2.6. Proper strain gauge bonding procedures 12
2.7. Proper strain gauge soldering procedures 13
CHAPTER III **14**
MODELING AND EXPERIMENTAL ANALYSIS OF THE EXPECTED OPERATION **14**
3.1. The strain gauge testing station 14
3.1.1. The electro-mechanical driving system 15
3.1.2. The data acquisition system 15
3.1.3. The data analysis software 16
3.1.4. Methodology: Obtaining measurements 16
3.1.5. Modeling 18
3.2. A mechanical approach for modeling the testing station 18
3.2.1. The guided cantilever 19
3.2.2. Beam bending equations of a cantilever 21
3.2.3. An example of ±1 mm oscillation 23
3.3. A geometrical approach for modeling the testing station 25
3.3.1. The geometry 25
3.3.2. Governing equations 26
3.3.3. An example of ±1 mm oscillation 27
3.4. The theoretical expected results 28
3.4.1. The time domain 29
3.4.2. The amplitude domain 30

3.4.3. The frequency domain 31
3.5. The experimental results 33
3.5.1. The time domain 33
3.5.2. The amplitude domain 37
3.5.3. The frequency domain 38
CHAPTER IV 40
MODELING AND EXPERIMENTAL ANALYSIS OF FAILURE MODES 40
4.1. Failure modes 40
4.2. Debonding model 42
4.2.1. Debonding model and theory 43
4.2.2. Example situations 45
4.2.3. Debonding results 47
4.3. Lead termination model 49
4.3.1. Lead termination model and theory 51
4.3.2. Example situation 53
4.3.3. Lead termination results 53
4.4. FMEA application 56
CHAPTER V 60
CONCLUSIONS AND RECOMMENDATIONS 60
5.1. Conclusions 60
5.2. Contributions 62
5.3. Recommendations for future work 62
LIST OF REFERENCES 65
APPENDIX A 70
APPENDIX B 73
APPENDIX C 74
APPENDIX D 75
APPENDIX E 77
VITA 80

LIST OF TABLES

Table 1: List of symbols and measurements.....xi
Table 2: List of abbreviations.....xii
Table 3: Geometrical model values 27
Table 4: Correction factor from an example set of data with different vertical displacements 36
Table 5: Measured decrease in amplitude during debonding..... 49
Table 6: Documentation of FMEA for strain gauge testing 58

LIST OF FIGURES

Figure 1: Typical uniaxial strain gauge 1
Figure 2: Example of cracking under HCF conditions [3] 2
Figure 3: Axial tension and compression 7
Figure 4: Strain gauge with labels 8
Figure 5: The Wheatstone bridge 11
Figure 6: The Vishay® EA-06-062AP-120 120Ω strain gauge 12
Figure 7: Strain gauge testing station flow chart 14
Figure 8: Dimensions and motion of the strain gauge electro-mechanical driving system 15
Figure 9: Methodology for obtaining results 17
Figure 10: A cantilever beam 19
Figure 11: A cantilever beam, guided at point A, fixed at point B 20
Figure 12: Range of beam deflection between ±1 mm 23
Figure 13: Strain with relation to beam deflection 24
Figure 14: Geometric dimensions of bending 25
Figure 15: $A_{mechanical}$ and $A_{geometrical}$ amplitudes at ±1 mm 28
Figure 16: Expected time domain signal 29
Figure 17: Histogram as a U-shaped distribution 31
Figure 18: Window function and time limited sine wave 32
Figure 19: Spectrum of windowed sine wave (A) and sampled spectrum of finite length sine wave (B) 32
Figure 20: 2 mm displacement 34
Figure 21: 1.5 mm displacement 34
Figure 22: 1 mm displacement 35
Figure 23: 0.5 mm displacement 35
Figure 24: Experimental correction factor 36
Figure 25: Measured amplitude domain versus 38
Figure 26: Measured frequency domain versus theoretical frequency domain 39
Figure 27: Vishay® strain gauge grid alignments 41
Figure 28: Ratio of debonded area to bonded area of grid 42
Figure 29: Ratio of bonded length to debonded length 43
Figure 30: Example signal of tension and compression 46
Figure 31: Peeling a gauge from the surface (A) and partial grid attachment (B) 46
Figure 32: Output voltage as a function of percentage of bonded area 47
Figure 33: Non-symmetric detection during tension and compression 48
Figure 34: Signal decrease in amplitude during debonding 48

Figure 35: Signal from strain gauge showing non-symmetric detection during tension and compression because of interior debonding 50
Figure 36: Theoretical model versus expected experimental results 52
Figure 37: Lead termination example: left lead terminating, right lead secure 53
Figure 38: Signal of strain gauge because of lead termination 54
Figure 39: Comparison of theoretical and experimental amplitudes of strain gauges with wire lead termination 55
Figure 40: Frequency spectrum of lead termination example 55
Figure 41: Strain gauge signals from later stages of lead termination (1) 57
Figure 42: Strain gauge signals from later stages of lead termination (2) 57
Figure 43: Bonding step 1 70
Figure 44: Bonding step 2 70
Figure 45: Bonding step 3 70
Figure 46: Bonding step 4 70
Figure 47: Bonding step 5 71
Figure 48: Bonding step 6 71
Figure 49: Bonding step 7 71
Figure 50: Bonding step 8 71
Figure 51: Bonding step 9 71
Figure 52: Bonding step 10 72
Figure 53: Bonding step 11 72
Figure 54: Bonding step 12 72
Figure 55: Soldering step 1 73
Figure 56: Soldering step 2 73
Figure 57: Soldering step 3 73
Figure 58: Soldering step 4 73
Figure 59: Signal conditioning circuit diagram 74
Figure 60: The signal conditioning circuit board 74
Figure 61: Tektronix CFG280 signal generator 75
Figure 62: Electro-mechanical driving system 75
Figure 63: Signal conditioning circuit 75
Figure 64: Digital oscilloscope 76
Figure 65: Computer 76

LIST OF SYMBOLS, MEASUREMENTS, AND ABBREVIATIONS

Table 1: List of symbols and measurements

Term	Symbol
Displacement	δ
Gauge factor	GF
Length	ℓ, L
Microstrain	$\mu\varepsilon$
Distance (millimeters)	mm
Voltage (millivolts)	mV
Moment of Inertia	I
Poisson's ratio	υ
Resistance (ohms)	R (Ω)
Resistivity (ohms-mm)	ρ
Strain	ε
Stress	σ
Time (milliseconds)	ms
Transverse direction	γ
Young's modulus of elasticity	E

Table 2: List of abbreviations

Abbreviation	Phrase
AEDC	Arnold Engineering Development Center
FMEA	Failure Modes and Effects Analysis
GF	Gauge Factor
HCF	High Cycle Fatigue
HTML	Hypertext Markup Language
PHP	Hypertext Preprocessor
SQL	Structured Query Language
UTSI	University of Tennessee Space Institute

CHAPTER I
INTRODUCTION AND MOTIVATION

1.1. Introduction

Strain is a measure of the deformation of a body caused by external forces. It is determined as the ratio of the change in length of a body to the original body length under an applied load. A resistance strain gauge, shown in Figure 1, is a sensor that measures strain in terms of a change in electrical resistance. It is bonded to a surface and intended to experience the same deformation as the body. Fundamentally, the strain gauge is a resistor whose resistance varies with respect to the amount of deformation to which it is subjected. Strain gauges convert a mechanical quantity, strain, into an electrical signal, resistance [1]. Strain gauge applications combine the knowledge and technology of mechanical and electrical concepts.

A common use for strain gauge measurements is aircraft component testing. Strain gauges are bonded along the surface of the critical component and report the stress generated by the machinery. The results are used to determine potential points of failure along the surface of the component [2]. Approximately 50% of all turbine engine failures are believed to occur because of high cycle fatigue, HCF [3]. Turbine engines, while operating in high vibration conditions, can experience HCF failure with little or no warning and with potentially catastrophic consequences [4].

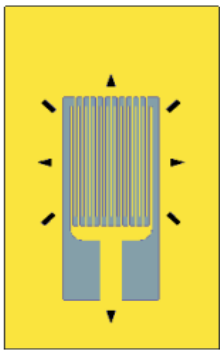


Figure 1: Typical uniaxial strain gauge

Research facilities, such as the United States Air Force's Arnold Engineering Development Center, AEDC, perform testing on turbine engine components to investigate durability during HCF situations. Testing is performed to understand the tradeoff between material strength and operational stability. Strain gauges are bonded at high stress locations and measure the strain during engine rotational acceleration and deceleration ramps, which result from engine throttle changes. The resulting measurements are used to identify potential weaknesses in component design. These strain measurements are critical to understanding the fatigue characteristics of the components during mechanical operation [5], [6].

The results measured by strain gauges sometimes fail to report the correct values of experienced strain or expected forms in the time, amplitude, and frequency domains.

In general, the first response when observing failure measurements is to investigate the component itself for failure. Different turbine engines are made with different materials of varying strength. A large amount of research is dedicated to understanding the metallographic and vibratory response of failed components because of HCF [3], [7]. Figure 2 shows an example of cracking on a blade surface resulting from a HCF condition [3]. Often, uncertainties in strain measurements are attributed to the gauge placements on a turbine blade. Much literature also exists on analyzing the ideal placement of strain gauges, as well as on detailed methods for determining the optimal strain gauge arrangement on a blade [8]. Even the effects of instrumentation location and failure must be suspected when observing unexpected results in strain gauge output.



Figure 2: Example of cracking under HCF conditions [3]

While extensive research has been performed to understand what happens when the component or instrumentation fails, little research has been conducted to understand what happens when the strain gauge itself fails during cyclic testing [5], [6]. Stress analysts must be able to rely on a sensor to generate correct strain values and also must be confident that the sensor is measuring the correct type of strain.

A failure mode is a situation in which a sensor, or any system, fails to meet the original intent of the design. Failure modes result in measuring unexpected signals, experiencing degraded performance or, in extreme cases, injury to or death of the user [9]. Failure Modes and Effects Analysis, FMEA, is a methodology for understand and characterizing failure modes of a product early in its development cycle. Each vendor has its own steps for analyzing FMEA results [9]. The research described here provides a means of performing FMEA testing on strain gauges to understand the potential failure characteristics and causes. In general, the FMEA steps undertaken in the research include:

1) Understand the product and the associated processes
2) Understand the processes subjected to the product
3) Generate block diagrams for each process
4) Develop a means of tracking of the data and other important information
5) Identify potential failure modes and their causes
6) Observe, describe, and report the effects of the failure modes

1.2. Objectives

The work presented in this thesis examined the technology and operation of a typical, modern, and often used resistance strain gauge. The equations that govern the operation of a strain gauge were derived and later applied to situations that may result in a failure mode. An experimental apparatus was constructed at the University of Tennessee Space Institute to generate mechanical motion for generating strain on a beam. Strain gauges were bonded to the surface of a cantilever beam which was then subjected to oscillations in the vertical plane. The resulting resistance changes were monitored and recorded for further analysis.

The primary goal of this research was to develop predictive models for strain gauge responses under controlled laboratory conditions. These models would effectively verify the use of the laboratory environment to generate failure characteristics of a

strain gauge. Applying the FMEA methodology to the strain gauge testing station resulted in six research objectives.

The first objective was to understand the product and the associated processes. The product, a Vishay® EA-06-062AP-120 strain gauge, was used to measure the axial strain along a bending cantilever beam. The technology and fundamental operation of a strain gauge was analyzed and later applied to situations resulting in failure modes. The associated processes, proper bonding and soldering procedures, were analyzed. The importance of each were established by demonstrating failure modes arising from improper bonding and soldering situations.

The second objective was to understand the processes to which the product was subjected. This was accomplished by modeling the behavior of a strain gauge in the testing station under normal, non-failure, operating conditions. The testing station was composed of an electro-mechanical driving system, a data acquisition system, and analysis software. The electro-mechanical driving system produced a sinusoidally-varying strain on a subject strain gauge. The data acquisition system recorded the results on a computer. Predictive models were developed by relating the mechanical motion of the testing station and classical beam bending analysis, as well as by approximating the shape of the station by geometrical means. The equations from each approach were used to relate the bending beam to the strain measured by a strain gauge. These models were later qualitatively and quantitatively applied to experimental results.

The third objective was to generate block diagrams of each process. These visualizations demonstrate the relationships between the individual steps and components of each process. Visual representations of each process as a block diagram provided an easy means of determining the source of a potential failure mode.

The fourth objective was to develop a means of storing and analyzing the experimental results. This was accomplished by developing data analysis software to store the results in a database and analyze the measurements by observing the results in the time, amplitude, and frequency domain. Failure mode indications of each domain were observed and experimentally verified.

The fifth objective was to identify potential failure modes and their causes. A failure mode is defined as any situation in which a strain gauge can potentially fail to measure correct strains. Some example situations were described that can cause strain gauges to

operate in failure modes, such as over-straining, operating outside of the temperature limits, physical and environmental damage, improper gauge selection, and improper bonding or soldering techniques.

The final objective was to observe, describe, and report the effects of failure modes of strain gauges. By understanding the operation of the testing station, failure modes were easily observed as signals that deviated from the expected results. Two particular failure modes, debonding and lead termination, were addressed and analyzed using the previous models developed for the strain gauge and testing station. Debonding occurred when the strain gauge began to peel from the surface or when the bond began to weaken over time. The signal experienced a loss in amplitude as well as some potential signal deformation. Wire lead termination occurred as the lead began to detach from the solder bead on the strain gauge. The resulting signal displayed signal deformation with amplitude loss and apparent frequency doubling. In rare cases, the resulting signal was so noisy that no predictive model was applied. In general, the termination point was modeled as an effective resistor in series with the strain gauge. These failure modes were produced in the laboratory setup to verify the models.

By the conclusion of this research, several goals were accomplished:

1) An analysis of strain gauge technology and fundamental operation was performed.
2) The workings of strain gauges were applied to develop predictive models of the electro-mechanical driving system by a mechanical approach and checked by a geometrical approximation approach.
3) The predictive models of the testing station were experimentally analyzed.
4) By understanding the fundamental operation of a strain gauge, as well as the expected results from the models of the driving system, predictive models of two potential failure modes, debonding and lead termination, were developed.
5) The predictive models of the failure modes were experimentally analyzed.
6) The strain gauge testing station was determined to be an effective laboratory facility for testing strain gauges under non-failure and failure operating conditions.

1.3. Outline

Chapter 1 provides an overview of this thesis as well as the objectives to be accomplished by this research. Chapter 2 is an explanation of the strain gauge

technology used for this research. This chapter begins by discussing the theory behind strain gauge operation and the proper handling procedures of strain gauge bonding and soldering. The Vishay® EA-06-062AP-120 strain gauge is investigated. Chapter 3 introduces the strain gauge testing station which is composed of an electro-mechanical driving system, a data acquisition system, and analysis software. It begins by discussing the components that make up the driving system. A brief description of the data acquisition system and the software used to analyze the strain gauge results is given. The driving system is then modeled by a mechanical and geometrical approach. Diagrams and the associated equations of each model are provided in the text. Once the models are explained, the methodology of this research is outlined. The experimental results are then compared with the theoretical results. Some theories are outlined to explain potential differences between the theoretical and experimental results. Chapter 4 begins by discussing several potential strain gauge failure modes. Two particular examples of failure modes, debonding and wire lead termination, are analyzed. This includes the theoretical models, derived from the results from Chapters 2 and 3, and the experimental measurements of strain gauges undergoing these particular failure modes. Finally, Chapter 5 states the conclusions and contributions of this research as well as recommendations for future research.

CHAPTER II
STRAIN GAUGE TECHNOLOGY

2.1. Mechanical strain

External forces applied to a body generate stress and strain on that body. Stress, σ, is a measurement of the internal resisting forces, while strain, ε, is the deformation of the body caused by the applied force, or the fractional change in length, ℓ, given by:

$$\varepsilon = \frac{d\ell}{\ell} \qquad Eq.2.1$$

Strain is a dimensionless value. Typically, magnitudes of strain values are quite small and are often expressed in terms of microstrain, or strain · 10^{-6} units [1]. Tension, or positive strain, causes the length of the surface to increase, the cross-sectional area of the surface to decrease, and the resistance of the strain gauge to increase. Conversely, compression, or negative strain, causes the length of the surface to decrease, the cross-sectional area of the surface to increase, and the resistance of the strain gauge to decrease [10]. This is illustrated in Figure 3.

For perfectly elastic materials, stress is related to strain by Hooke's Law, given by:

$$E = \frac{\sigma}{\varepsilon} \qquad Eq.2.2$$

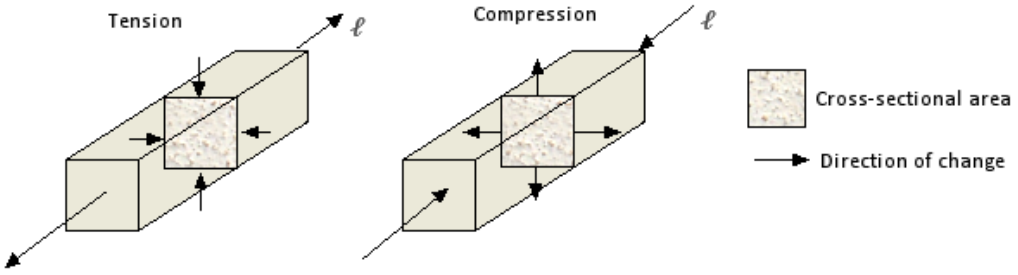


Figure 3: Axial tension and compression

where E is a material constant known as Young's Modulus, or the modulus of elasticity. This is the measure of how much force is needed to generate a unit deformation [11].

There are three different kinds of strain. Shearing strain is generated when angular distortion occurs to a body. Axial, or longitudinal, strain is defined as the ratio of the change in length of the wire, $d\ell$, to the length of wire, ℓ, as shown in Eq. 3. As a body changes in length, it also changes in cross-sectional area, as shown in Figure 3. Poisson's ratio is the negative ratio of transverse strain to longitudinal strain [12]. This research focuses only on longitudinal and transverse strain. Poisson's ratio relating longitudinal and transverse strain is given by:

$$\upsilon = -\frac{\varepsilon_\gamma}{\varepsilon_\ell} \qquad Eq.\,2.3$$

2.2. The resistance strain gauge

A resistance strain gauge is a sensor for measuring the deformation of a body in terms of an electrical signal. It is essentially a variable resistor that changes with respect to deformation, or strain, of a surface caused by an applied force. The strain gauge relates a mechanical quantity, strain, to an electrical quantity, resistance. The basic resistance strain gauge, shown in Figure 4, consists of a carrier, or the flexible backing, two large solder tabs, and a conductive wire arranged in a grid. The carrier provides the strain gauge with a surface ready for bonding to a test specimen and insulation between the conductive wire and the test specimen [13]. The length of wire is arranged in a grid orientation to maximize the length of wire in a particular axial direction. The strain is detected in the direction of the grid lines, called the longitudinal direction.

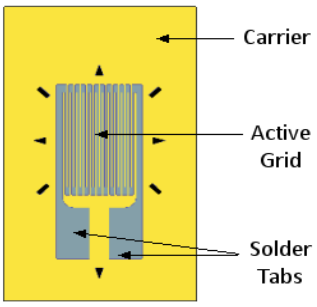


Figure 4: Strain gauge with labels

A strain gauge is attached, or bonded, to a testing specimen with a strong adhesive to transfer the physical characteristics of a surface to the gauge. This bonding adhesive allows the active grid to experience the same strain as the surface. A proper bond is essential to observe the actual strain on the testing specimen. A partial bond will not transfer all of the characteristics of the surface to the gauge [14]. As the surface changes in length, a strain is generated by Eq. 2.1. The changing strain at the location of the active grid causes a subsequent change in the resistance across the two solder terminals from the nominal resistance, R, given by:

$$dR = R \cdot GF \cdot \varepsilon \qquad Eq. 2.4$$

This change in resistance is generally quite small and requires an amplifier to change it into an acceptable magnitude [10].

Each strain gauge has an associated fundamental value called the gauge factor, GF. This is a dimensionless quality used to determine the sensitivity of the strain gauge to strain. Ideally, the strain gauge resistance depends only on strain; however material properties can also affect the resistance. The gauge factor is the ratio of the resistive rate of change to the longitudinal strain, given by:

$$GF = \frac{dR/R}{\varepsilon_\ell} \qquad Eq. 2.5$$

The value of the gauge factor is usually provided by the vendor. This value is experimentally determined using International Standard NAS 942, in which the strain gauge is bonded at room temperature to a beam designed for constant uniaxial stress. The beam has a Poisson's ratio of 0.285 and is subjected ±1500 microstrain [15].

2.3. Fundamental operation of a strain gauge

Fundamentally, a strain gauge has a nominal resistance resulting from the properties of the wire in the active grid. The conductive wire of the strain gauge generates the resistance detected across the solder tabs. The wire grid has end caps at the top and bottom of each segment. The end caps and solder tabs are considered insensitive to strain because of their relatively large cross-sectional area and low electrical resistance [16]. The wire is assumed to have a rectangular cross-sectional area with width, w, and height, h. An unstressed length of wire creates a nominal resistance, given by:

$$R = \frac{\rho \cdot \ell}{w \cdot h} \qquad Eq.\,2.6$$

where R is the resistance, ρ is the resistivity of the wire, ℓ is the length of the wire, and w·h is the cross-sectional area of the wire [12].

Stretching or compressing the wire changes the values that determine this resistance. The resistance changes as a combination of changing length, cross-sectional area, and resistivity, given by:

$$dR = \frac{\rho}{w \cdot h} d\ell - \frac{\rho \cdot \ell}{(w \cdot h)^2} dh - \frac{\rho \cdot \ell}{(w \cdot h)^2} dw + \frac{\ell}{w \cdot h} d\rho \qquad Eq.\,2.7$$

Dividing Eq. 2.7 by Eq. 2.6, an expression of the resistive rate of change is found:

$$\frac{dR}{R} = \frac{d\ell}{\ell} - \frac{dh}{h} - \frac{dw}{w} + \frac{d\rho}{\rho} \qquad Eq.\,2.8$$

Applying Poisson's ratio from Eq. 2.3 to the change in height and width and the definition of longitudinal strain, the resistive rate of change is modified:

$$\frac{dR}{R} = \varepsilon_\ell - \varepsilon_\gamma - \varepsilon_\gamma + \frac{d\rho}{\rho} \qquad Eq.\,2.9$$

$$\frac{dR}{R} = (1 + 2 \cdot \upsilon) \cdot \varepsilon_\ell + \frac{d\rho}{\rho} \qquad Eq.\,2.10$$

Comparing Eq. 2.5 to Eq. 2.10 shows that the gauge factor of a strain gauge is

$$GF = 1 + 2 \cdot \upsilon + \frac{d\rho/\rho}{\varepsilon_\ell} \qquad Eq.\,2.11$$

The gauge factor is determined by Poisson's ratio, the resistivity rate of change, and the longitudinal strain [12], [17].

2.4. The Wheatstone bridge

A strain gauge requires a conditioning circuit that can accurately measure very small changes in resistance. This is accomplished with a quarter-circuit Wheatstone bridge. In Figure 5, the R3 resistor is the strain gauge. To create a zero voltage, the bridge is symmetrically balanced by setting R1 and R2 equal, and adjusting the R4 resistor to equal the R3 strain gauge resistance. A voltage, V_{out}, is generated when the R3 resistor changes, thus causing the bridge to become unbalanced [18].

The output voltage in terms of the resistances and the excitation voltage, V_{ex}, is given by:

$$V_{out} = V_{ex} \cdot \left[\frac{R3}{R3 + R4} - \frac{R2}{R1 + R2}\right] \qquad Eq.\,2.12$$

where R3 is the strain gauge resistance and R4 is the rheostat arm resistance adjusted to balance the bridge. The voltage is also expressed in terms of the gauge factor and strain, given by [10], [18]:

$$V_{out} = \frac{V_{ex}}{4} \cdot \frac{GF \cdot \varepsilon_\ell}{1 + GF \cdot \frac{\varepsilon_\ell}{2}} \qquad Eq.\,2.13$$

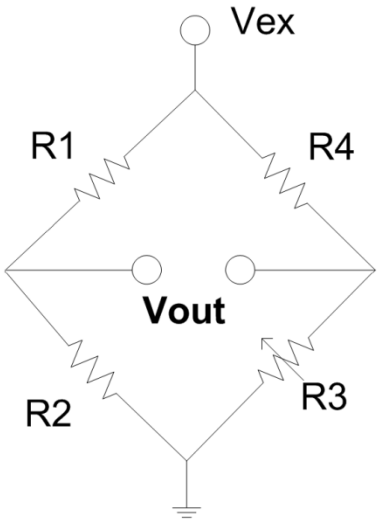


Figure 5: The Wheatstone bridge

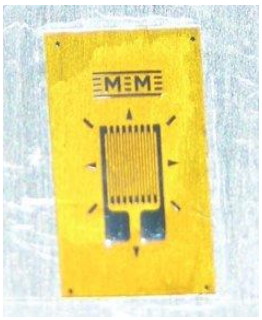


Figure 6: The Vishay® EA-06-062AP-120 120Ω strain gauge

2.5. The Vishay® EA-06-062AP-120 120Ω strain gauge

The Vishay® EA-06-062AP-120 120Ω strain gauge, shown in Figure 6, was chosen for its ability to analyze general-purpose static and dynamic experiments. This strain gauge has a nominal resistance of 120Ω ± 0.15% and a gauge factor of 2.035 ± 0.5%. The normal operating temperature ranges from -100 ^{o} to 350 ^{o} F; however, it may operate for short periods of time from -320 ^{o} to 400 ^{o} F. It provides moderate accuracy and is not recommended for experiments requiring high accuracy [15], [19].

The EA-06-062AP-120 strain gauge has a flexible, polyimide carrier and a constantan foil active 90^{o} rosette grid. The constantan provides a resistivity of 0.49 μΩ·m and a near constant sensitivity to strain [20]. The surface area of the strain gauge carrier measures approximately 4.1 mm by 6.6 mm, with a surface area of 1.57 mm by 1.57 mm for the active grid. It also has solder tabs measuring approximately 0.6 mm by 0.6 mm [15].

2.6. Proper strain gauge bonding procedures

Bonding a strain gauge to a surface is a difficult process. Bonding, or gauging, in essence, is gluing a strain gauge to the testing surface in a location that will produce tension and compression at the location of the strain gauge grid. Improper installation of a strain gauge can lead to inaccurate results or unstable measurements [18]. A successful bond transfers all of the surface characteristics to the gauge [14]. In the technique used in this research, the first step was to prepare the surface of an aluminum beam for bonding. This required degreasing the surface with isopropyl alcohol and abrading the surface with grit silicon-carbide paper. This action created a smooth bonding surface free of residue and contaminants that can adversely affect the bonding process. Once the surface was prepared, the strain gauge was positioned in the proper location with a piece of clear tape. The bonding agent, M-Bond 200, creates a

strong connection between the strain gauge and the testing surface when it comes in contact with a catalyst. The liquid catalyst was applied to the back of the carrier and a small amount of the adhesive was applied to the testing surface. Next, the tape was lowered onto the testing surface so that adhesive came into contact with the catalyst. Pressure was applied to the top of the strain gauge for approximately two minutes and a secure connection was made. After the tape was peeled away, the strain gauge was ready to be connected to the conditioning circuit [21]. Improper bonding sometimes led to invalid measurements and certain failure modes, as will later be shown. Complete instructions for properly bonding strain gauges to a surface can be found in Appendix A.

2.7. Proper strain gauge soldering procedures

Once the strain gauge was successfully bonded to the testing surface, it was connected in series with the conditioning circuit. Two 8 inch 34 AWG copper wires connected the strain gauge to the conditioning circuit. One end of each wire was connected to the Wheatstone bridge. The other end of each wire was soldered onto each solder tab of the strain gauge. Since the strain gauge is very small, using a significant amount of flux was necessary to create a good solder bead. Vishay® M-Flux AR activated rosin soldering flux was used. First, a solder bead was built up on each solder tab of the strain gauge. Afterwards, the lead was melted into the solder bead with the soldering iron. The Vishay® M-Line rosin solvent was then used to neutralize the residual flux, within two minutes of application [22], [23]. Improper soldering also sometimes led to certain failure modes, as will later be shown. Complete instructions for properly soldering the leads to the strain gauge can be found in Appendix B.

CHAPTER III
MODELING AND EXPERIMENTAL ANALYSIS OF THE EXPECTED OPERATION

3.1. The strain gauge testing station

The strain gauge testing station was composed of an electro-mechanical driving system, a data acquisition system and the analysis software. The electro-mechanical driving system applied a force to deflect a beam, thus generating a time-varying strain to a subject strain gauge mounted on a testing surface. The data acquisition system was designed to obtain strain values from the electro-mechanical driving system. Measurements were recorded and saved on a computer. The data analysis software was then used to observe and analyze the results. This was accomplished by generating plots and calculating statistical and experimental values. Figure 7 shows the movement of data through the strain gauge testing station.

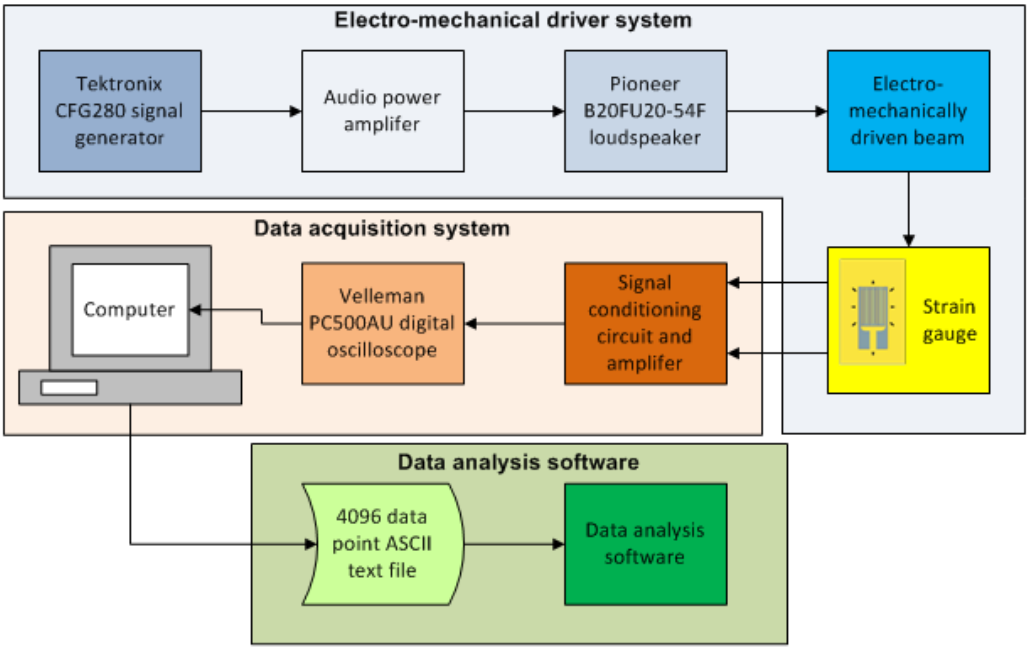


Figure 7: Strain gauge testing station flow chart

3.1.1. The electro-mechanical driving system

The electro-mechanical driving system produced a sinusoidally-varying strain on a subject strain gauge. A Tektronix CFG280 signal generator drove a 7-watt audio power amplifier with a sinusoidal signal at a particular user-defined amplitude and frequency. This in turn drove a Pioneer B20FU20-54F audio loudspeaker. A rod extended from the speaker to a 382 mm long, 25 mm wide, 3 mm thick flexible aluminum beam. This aluminum beam was secured on one end by an aluminum block and secured to the rod by wing nuts 250 mm from the block. The block created an effective beam length of 325 mm. A strain gauge was bonded to the surface by following the process outlined in Appendix A at a point 25 mm from the block. The loudspeaker caused the beam to oscillate vertically. The vertical displacement was measured with a precision caliper 100 mm from the aluminum block. The strain gauge was bonded about a center point located 25 mm from the aluminum block. Figure 8 shows the dimensions of the mechanical drive system and the shape of the beam.

3.1.2. The data acquisition system

Two wires from the solder tabs connected the strain gauge to the signal conditioning circuit. The signal conditioning circuit, designed and built at UTSI by Dr. Bruce Bomar, consisted of a quarter-circuit Wheatstone bridge and an amplifier. The excitation

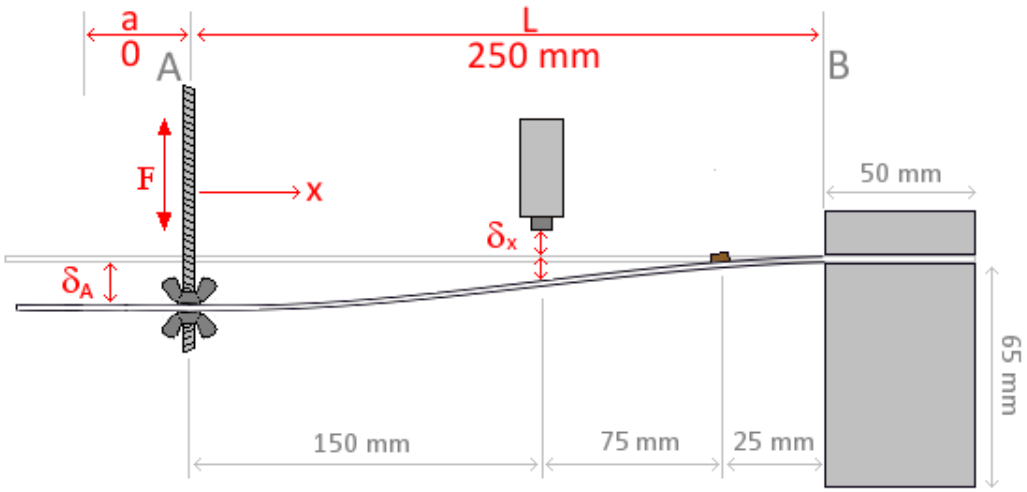


Figure 8: Dimensions and motion of the strain gauge electro-mechanical driving system

voltage of the bridge was 3.3V. The amplifier gain was set to 522 by setting the R3 potentiometer to 11.5Ω. The strain gauge measurements were acquired by a Velleman® PC500AU PC-based oscilloscope and displayed on a computer monitor. Data was stored on the computer as software generated ASCII text files for post-acquisition analysis [5]. The circuit diagram of the signal conditioning circuit, designed by Dr. Bomar, is found in Appendix C. A detailed flowchart for the strain gauge testing station is found in Appendix D.

3.1.3. The data analysis software

In order to understand and compare the results from each strain gauge, a software solution was developed to manage and view the data. This software was a website interface programmed with HTML, PHP, and SQL. After each test setting, an ASCII text file was generated and saved onto the computer. Each file contains the oscilloscope settings and two sets of 4,096 data points; one for the driving signal and one for the measured strain gauge results. The file was then uploaded into a database for further analysis.

This software utilized PHPLOT, open source software for plotting graphs, to display the plots for each test setting [24]. Measurements were displayed in the time, amplitude, and frequency domains. Each set of results could be compared to any set by averaging two signals, taking the difference of two signals, or displaying both signals at the same time. Statistical properties, such as maximum value, minimum value, mean, median, and range, were calculated. Experimental values, such as the RMS voltage and peak-to-peak voltage, were also calculated for comparison between different signals. This website interface provided a simple solution to view the results and focus on particular areas of interest for this research.

3.1.4. Methodology: Obtaining measurements

The beam was first prepared for strain gauge attachment by following the proper bonding techniques, outlined in Section 2.6. A strain gauge was then bonded to the beam and the wires were soldered onto the solder tabs. The beam was secured into the testing station with wing nuts on one end and an aluminum block clamp on the other. The fasteners were fixed finger tight. The wires were then connected in series with the conditioning circuit through conductive screws mounted on the side of the testing station. The R5 resistor was a potentiometer used to adjust the rheostat arm. Prior to each test, the circuit was calibrated to balance the Wheatstone bridge.

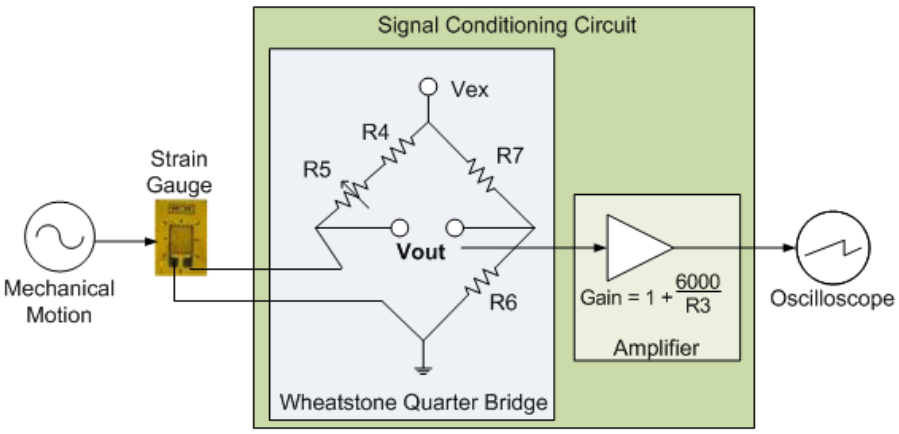


Figure 9: Methodology for obtaining results

The signal generator for the beam motion driving was set to a particular frequency and amplitude. It generated the sinusoidal driving signal to the audio amplifier and loudspeaker. The audio amplifier amplitude was adjusted to achieve a particular vertical displacement, measured by a precision caliper. The loudspeaker motion generated a cyclic, mechanical motion creating a vertical deflection along the beam, measured at a point 100 mm away from the block. The strain gauge experienced the strain on the surface of the beam at a point 25 mm from the block. The local tension and compression of the surface caused the resistance of the strain gauge to increase and decrease accordingly. Figure 9 illustrates this process with the resistance values indicated in the circuit diagram. On the signal conditioningcircuit board, the Wheatstone bridge generated an output voltage from the measured change in resistance, dR. The voltage equation, Eq. 2.12, was modified to reflect the actual values on the conditioning circuit board.

$$V_{out} = V_{ex} \cdot \left[\frac{R_{nominal} + dR}{R_{nominal} + dR + R4 + R5} - \frac{R6}{R6 + R7}\right] \qquad Eq.3.1$$

where V_{ex} was 3.3V, $R_{nominal}$ was 120Ω, R4+R5 was adjusted to 120Ω, and R6 and R7 were 1000Ω. This output voltage was then amplified with a gain determined by the value of the R3 potentiometer, given by:

$$G = 1 + \frac{6000}{R3} \qquad Eq.3.2$$

The oscilloscope displayed a voltage with respect to time, given by:

$$V_{oscilloscope} = V_{out} \cdot G \qquad Eq.3.3$$

The measurement settings of the oscilloscope remained the same throughout all of the strain gauge testing. The first channel on the oscilloscope was set to 0.15 volts per division for the strain gauge output. The second channel on the oscilloscope was set to 50 mV per division for the signal generator. The time setting was set to 20 ms per division. The oscilloscope was set to trigger on the leading edge of the driving channel and to be DC coupled.

After measurements for each strain gauge setting were recorded, a data file was saved to the computer and uploaded into the data analysis software. Strain gauge settings were observed and compared against each other for differences and similarities.

3.1.5. Modeling

Before observing a strain gauge operating in a failure mode, it was necessary to understand the behavior of the gauge in the testing station under normal, non-failure operating conditions. The following predictive models were developed to explain the relationship between the mechanical motion of the testing station and the strain gauge response to a sinusoidally-varying strain. After the theoretical models were developed, the strain gauge was ready to be subjected to failure conditions. Subsequent failure modes were observed because they did not follow the predictive models, derived as a mechanical model of classical beam bending analysis and checked by a geometrical approximation.

3.2. A mechanical approach for modeling the testing station

To understand how strain is generated on the surface of a beam, it is important to understand the mechanical properties of a bending beam. Beam bending analysis is based on the Euler-Bernoulli Equation, which combines concepts from kinematic, constitutive, force resultant, and equilibrium theories. Kinematics defines how a beam deflects with relation to its geometrical dimensions. Constitutive equations describe how stress and strain are related in a beam by Hooke's and Poisson's Laws. Force resultant equations describe how the force is transmitted in a beam. This includes the stress experienced by a beam in regards to forces, moments, and reactions. The

equilibrium equations relate the internal stresses to the external loads [25]. Combining all of these theories gives the Euler-Bernoulli beam equation, given by:

$$\frac{d^2}{dx^2}\left[E \cdot I \cdot \frac{d^2w}{dx^2}\right] = p(x) \qquad Eq.3.4$$

where E is the Young's modulus of elasticity, I is the moment of inertia, x and w define dimensional properties, and p is the distributed loading on the beam. The following derivations of beam bending are based on the original assumptions and derivations defined by the Euler-Bernoulli analysis [25]. This model uses an aluminum beam.

3.2.1. The guided cantilever

A cantilever, Figure 10, is defined as a beam that is supported and fixed at one end and supports a load at the other end [26]. The motion of the electro-mechanical driving system can be described as an oscillating cantilever, fixed on one end, and guided on the other [27]. In Figure 8, the beam is fixed at point B and projects out into space. A force is applied at point A on the opposite side of the beam that causes the beam to bend. Stresses and strains are exerted on the beam resulting from the external forces. In general, strain occurs in multiple dimensions and can be observed as many different kinds of strain. Figure 10 illustrates the motion of a basic cantilever.

Many factors must be considered for when modeling the strain gauge testing station as a cantilever. The elasticity of the beam, cross sectional area, load on the beam, and the location of the load will each contribute to the motion of a cantilever. The support of

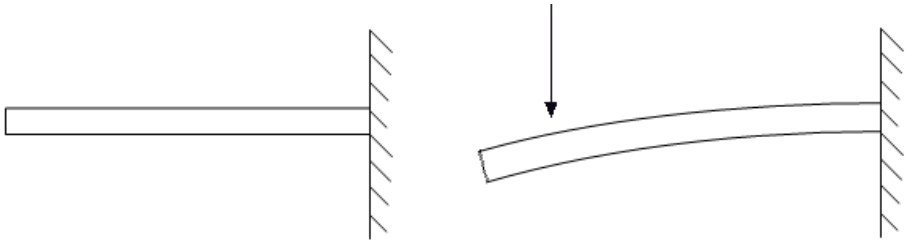


Figure 10: A cantilever beam

the beam will determine the boundary conditions associated with the cantilever [28]. Young and Budynas have provided the derivations for the equations that define a cantilever [29]. The following model examines the most basic aspects of strain in the axial direction.

Some sign and unit conventions were associated with the cantilever motion and signal conditioning circuit. All measurements of length and deflection were in millimeters, mm. Vertical deflections were positive upward. Horizontal distances were positive to the right. The horizontal origin of the beam was located at point A. All forces were in Newtons, N. Downward forces were positive, while upward forces were negative. Strain is dimensionless; however references to it were in microstrain, $\frac{mm}{mm} * 10^{-6}$. A positive force created a downward motion in the beam and tension on the strain gauge. Tensile strain was positive. A negative force created an upward motion in the beam and compression on the strain gauge. Compressive strain was negative. Moments that bend the beam convex downward were positive, while moments that bend the beam convex upward were negative. Reactions were positive upwards.

Figure 11 illustrates the motion and forces acting on a cantilever beam, guided at point A and fixed at point B, provided by [29]. A load, F, is applied at point A that causes the beam to bend a vertical deflection, δ, at any point, x, along the beam. The beam protrudes from the fixed end, causing the slope at point B to be zero. The region of interest for the shape of the beam begins at the loading point and extends to the fixed point at B. For this reason, the value of a is zero. This model assumes that the slope at point A is also zero, where the wing nuts secure the rod from the loudspeaker to the beam. For this reason, a left end guided, right end fixed model of a cantilever was required [27].

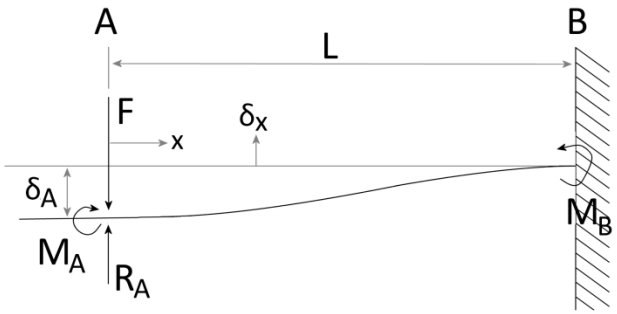


Figure 11: A cantilever beam, guided at point A, fixed at point B

The boundary conditions and physical properties of the cantilever are given by [27]. Since this is a guided cantilever, the reaction at A, the slope at A, and the slope at B are all zero. The reaction at B, R_B, is the same as the force that is being applied. The moments at A and B, M_A and M_B, are given by [29]:

$$M_A = F \cdot \frac{(L-a)^2}{2 \cdot L} \qquad M_B = F \cdot \frac{(L^2 - a^2)}{2 \cdot L} \qquad Eq. 3.5$$

The aluminum beam has a length, L, of 250 mm, a width, w, of 25 mm, and a height, h, of 3 mm. The distance from the top of the beam to the neutral axis, c, is half of the height of the beam, 1.5 mm. The region of the beam to the left of the point where the load is applied is of no interest because the vertical deflection is assumed to remain the same. The modulus of elasticity, E, of the beam is $10 \cdot 10^6$ psi, or 68927 $\frac{N}{mm^2}$ [30]. The moment of inertia, I, of the beam is 56.25 mm^4, and is given by:

$$I = \frac{1}{12} w h^3 \qquad Eq. 3.6$$

3.2.2. Beam bending equations of a cantilever

For a guided cantilever, [27] provides the deflection at point A, given by:

$$\delta_A = -\frac{F}{12EI} \cdot (L-a)^2 \cdot (L+2a) \qquad Eq. 3.7$$

By rearranging Eq. 3.7, the force is given by:

$$F = -\frac{12 \cdot \delta_A \cdot E \cdot I}{(-L+a)^2 \cdot (L+2 \cdot a)} \qquad Eq. 3.8$$

[27] gave the vertical deflection of the beam at any point, x, given by:

$$\delta_x = \delta_A + \theta_A x + \frac{M_A x^3}{2EI} + \frac{R_A x^3}{6EI} + \frac{F}{6EI}(x-a)^3 \qquad Eq. 3.9$$

Applying the boundary conditions and Eq. 3.8 to this relationship, this equation was simplified and rearranged as a function of δ_x to find δ_A.

$$\delta_A = \frac{\delta_x L^2}{L^3 - 3Lx^2 + 2x^3} \qquad Eq.\,3.10$$

This provided a means of viewing the deflection of the beam at any point given a known δ_A. The displacement at any point on the beam is given by:

$$\delta(x) = \delta_A - \frac{3 \cdot \delta_A \cdot x^2}{L^2} + \frac{2 \cdot \delta_A \cdot x^3}{L^3} \qquad Eq.\,3.11$$

The strain at any point on the beam was determined by finding the bending moment of the beam at any point. [27] gives the bending moment of a cantilever as:

$$M_x = M_A + R_A x - F(x - a) \qquad Eq.\,3.12$$

The R_A and a terms are zero, leaving the bending moment as a function of the location along the beam. Applying the boundary conditions and a known displacement at the location of the caliper provides the bending moment as a function of vertical displacement at the caliper and location along the beam, x, given by:

$$M_x = \frac{6 \cdot \delta_x \cdot E \cdot I \cdot (L - 2 \cdot x)}{L^3 - 67500 \cdot L + 6750000} \qquad Eq.\,3.13$$

The properties of elastically deforming beams relate the bending moment to stress, σ. The bending stress at a point along the beam is given by:

$$\sigma_x = -\frac{M_x h}{2 \cdot I} \qquad Eq.\,3.14$$

where h is the thickness of the beam, 3 mm. Using the properties of the beam, the bending moment, and Hooke's Law from Eq. 2.2 to relate stress and strain, the strain, measured in microstrain, at any point along the beam, x, in terms of the vertical displacement at the caliper, is given by:

$$\varepsilon(x) = \frac{3 \cdot 10^6 \cdot \delta_x \cdot h \cdot (L - 2 \cdot x)}{L^3 - 6.75 \cdot 10^4 \cdot L + 6.75 \cdot 10^6} \qquad Eq.\,3.15$$

Applying the length and height of the beam provides the strain in microstrain:

$$\varepsilon(x) = 1.63636 \cdot \delta_x \cdot (250 - 2 \cdot x) \qquad Eq. 3.16$$

where h is the height of the beam, L is the length of the beam, and δ_x is the displacement measured at 150 mm. The strain gauge was located at a point 225 mm from the load. The strain on the surface was converted to a change in resistance, given by:

$$dR = R_{nominal} \cdot \varepsilon(x) \cdot GF \qquad Eq. 3.17$$

Applying the nominal resistance of the strain gauge, 120Ω, and the gauge factor, 2.035, the approximate change in resistance in ohms is given by:

$$dR = 400 \cdot \delta_x \cdot (250 - 2 \cdot x) \cdot 10^{-6} \qquad Eq. 3.18$$

3.2.3. An example of ±1 mm oscillation

Imagine that the beam is oscillating with a vertical displacement of ±1 mm at the measuring caliper, at x = 150 mm. The frequency of the signal generator was set to 25 Hz. Solving Eq. 3.10 gives the vertical displacement at the point of the applied load as -2.841 mm when δ_x is -1 mm and 2.841 mm when δ_x is 1 mm. Remember that negative displacement creates tension and positive displacement creates compression. Using 3.11, a plot of the beam deflection curve is shown for δ_x increments of 0.25 mm between ±1 mm. Figure 12 shows the expanded beam deflection curves.

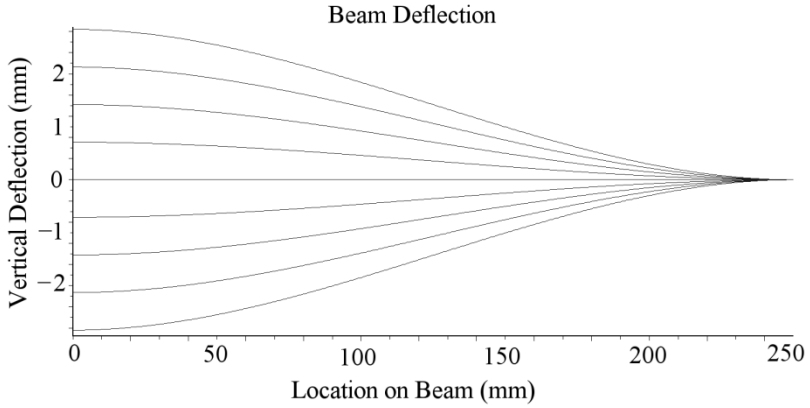


Figure 12: Range of beam deflection between ±1 mm

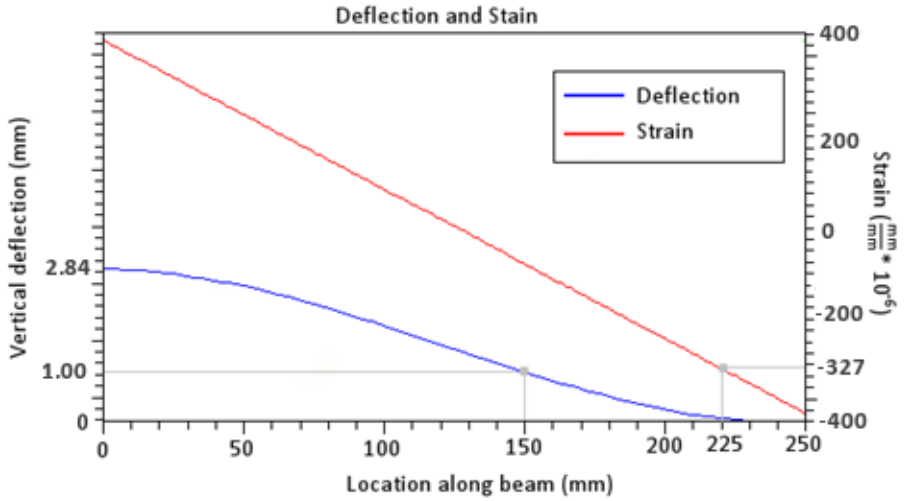


Figure 13: Strain with relation to beam deflection

Once the shape of the beam was determined, the stress at any point along the surface was found. From Eq. 3.15, the strain is found to be -327.273 microstrain at the point of highest compression and 327.273 at the point of highest tension. Figure 13 illustrates the strain along the upper surface of the beam with relation to the shape of the beam deflection, when δ_x is 1 mm. The left axis displays the height of the beam deflection. The right axis displays the magnitude of the strain values.

These strain values translate into a resistance measured by the strain gauge, given by Eq. 3.15. The resistance change, dR, at the point of highest compression is approximately -0.08Ω. The resistance change at the point of highest tension is approximately 0.08Ω. These resistances are applied to the Wheatstone bridge, Eq. 3.1, and amplifier, Eq. 3.2, to generate approximate output voltages of -287 mV at the point of highest compression and 287 mV at the point of highest tension.

In general, combining the Wheatstone bridge voltage, Eq. 3.1, and the change in resistance, Eq. 3.18, when experiencing a $\pm\delta_x$ displacement, the output voltage has an amplitude, $A_{mechanical}$, in mV, approximately given by:

$$A_{mechanical} = -285 \cdot x \qquad Eq. 3.19$$

3.3. A geometrical approach for modeling the testing station

The cantilever approach determined the output by examining the stress that the beam is undergoing at a particular point. From the stress, the strain and corresponding output voltage were found. This approach was checked by a simple geometrical approximation. A geometrical approach approximated the strain by measurements of distance only in relation to the shape of the bending beam as an arc.

3.3.1. The geometry

In Figure 14, the broken line, L_c, represents the original length of the beam from the aluminum block to the measuring caliper, 100 mm. The neutral axis of the bending beam remains the same length. However, the top of the beam, L_{top}, and the bottom of the beam change length during bending. The beam experiences a vertical displacement, δ_x, measured at the point of the caliper. The arc radius, r, is measured to the point of the neutral axis. The angle, θ, represents the arc angle of the beam curvature. This angle can be applied to both the original length, L_c, and the length of the top of the beam, L_{top}.

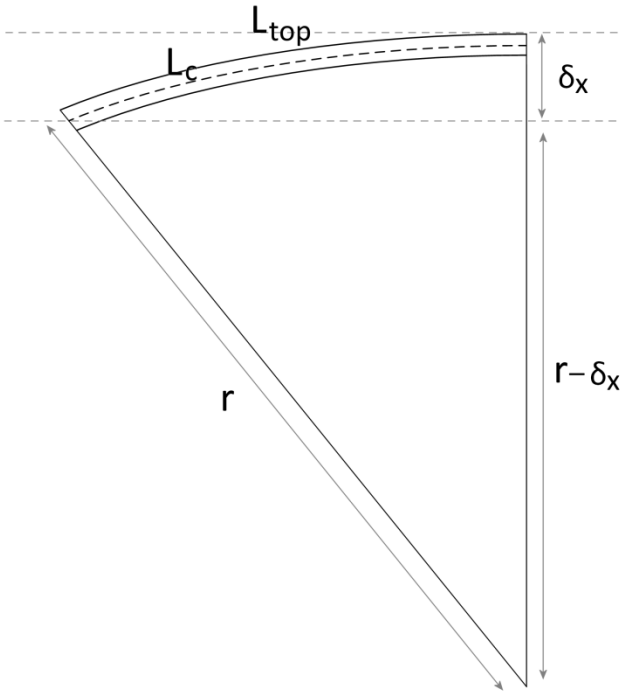


Figure 14: Geometric dimensions of bending

3.3.2. Governing equations

The original length of the neutral axis, L, is given by the definition of an arc length, given by:

$$L_c = \theta \cdot r \qquad Eq.\,3.20$$

The arc angle was determined from the trigonometric cosine relationship, given by:

$$\cos\theta = \frac{r - \delta_x}{r} \qquad Eq.\,3.21$$

Combining Eq. 3.20 and 3.21, a term for θ was found:

$$\frac{1 - \cos\theta}{\theta} = \frac{\delta}{L_c} \qquad Eq.\,3.22$$

For small values of theta, the following approximation is assumed true.

$$\cos\theta = 1 - \frac{\theta^2}{2} \qquad Eq.\,3.23$$

Applying this to Eq. 3.22, gave a term for the arc angle.

$$\theta = \frac{2 \cdot \delta_x}{L} \qquad Eq.\,3.24$$

Substituting this back into Eq. 3.20 gave a term for the arc radius.

$$r = \frac{L_c^2}{2 \cdot \delta_x} \qquad Eq.\,3.25$$

The new length of the top of the beam, L_{top}, is also an arc with the same arc angle, θ, described in Eq. 3.24. However, the new arc radius is the same arc radius described in Eq. 3.25 plus a thickness term. The thickness term is half the thickness of the beam, 1.5 mm. The new arc radius was measured to the top of the beam rather than the neutral axis.

$$L_{top} = \theta \cdot \left(r + \frac{h}{2}\right) \qquad Eq.\,3.26$$

The approximate strain can be calculated in terms of vertical displacement at the caliper, δ_x, given by:

$$\varepsilon = \frac{L_{top} - L_c}{L_c} \qquad Eq.\,3.27$$

$$\varepsilon = -\frac{h \cdot \delta_x}{L_c^2} \qquad Eq.\,3.28$$

$$\varepsilon = -300 \cdot \delta_x \qquad Eq.\,3.29$$

3.3.3. An example of ±1 mm oscillation

L_c is the length of the beam between the aluminum block and the measuring caliper, 100 mm, and T is the thickness of the beam, 3 mm. For a vertical oscillation, δ, of ±1 mm, θ and r were first found by Eq. 3.24 and Eq. 3.25. Then the length of the top of the beam, L_{top}, was found by Eq. 3.26. Table 3 shows the calculated values for an oscillation of ±1 mm.

From Eq. 3.29, the strain is found to be approximately -300 microstrain at the point of highest compression and approximately 300 at the point of highest tension. These strain values translate into a resistance measured by the strain gauge, given by Eq. 3.17. The

Table 3: Geometrical model values

δ (mm)	θ (degrees)	r (mm)	L_{top} (mm)	ε (microstrain)
1	0.02	5000	100.03	300
0.75	0.015	6666.67	100.0225	225
0.5	0.01	10000	100.015	150
0.25	0.005	20000	100.0075	75
0	-	-	100	0
-0.25	-0.005	-20000	99.9925	-75
-0.5	-0.01	-10000	99.985	-150
-0.75	-0.015	-6666.67	99.9775	-225
-1	-0.02	-5000	99.97	-300

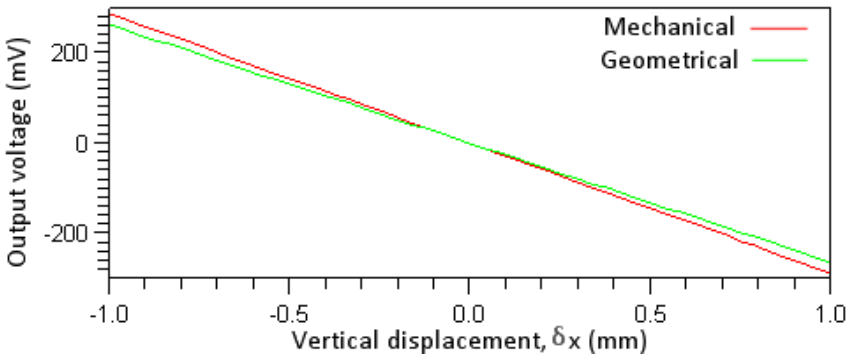


Figure 15: $A_{mechanical}$ and $A_{geometrical}$ amplitudes at ±1 mm

resistance change, dR, at the point of highest compression is approximately -0.073Ω. The resistance change at the point of highest compression is approximately 0.073Ω. From Eq. 3.1 and 3.2, the approximate output voltages of -263 mV at the point of highest compression and 263 mV at the point of highest tension.

In general, with regards to geometrical strain, Eq. 3.29, during a $\pm\delta_x$ displacement, the output voltage has an amplitude, $A_{geometrical}$, in mV, approximately given by:

$$A_{geometrical} = -262 \cdot x \qquad Eq.3.30$$

Figure 15 shows the voltage amplitudes, $A_{mechanical}$ and $A_{geometrical}$, in relation to a vertical oscillation, δ_x, between -1 mm and 1 mm.

3.4. The theoretical expected results

Once the models for the electro-mechanical driving system were developed, it was necessary to understand the plots that were expected to be generated during normal operation. These theoretical expectations were compared to the measured results for model verification, as will later be shown. By understanding the expected signals, it was assumed that failure modes could be observed as deviations from these expected results. The actual measured results were analog-to-digital discrete values that have been quantized by a digital oscilloscope with 8-bit resolution. The theoretical results were derived in continuous-time to easily calculate and visualize the different domains, including:

1) The time domain – observe the signal amplitude with respect to time.

2) The amplitude domain – observe the histogram, frequency that the signal attains a particular value.
3) The frequency domain - how much of the signal lies within each given frequency band over a range of frequencies [32].

3.4.1. The time domain

The electro-mechanical driving system was driven by a sinusoidal signal. The sinusoidal driving signal generated a sinusoidal cyclic, vertical motion of the beam. As demonstrated in the models outlined in this chapter, the output voltage was expected to oscillate sinusoidally between two amplitudes, ±A. This was approximated by a continuous-time sine wave, given by:

$$y = A \cdot \sin(2 \cdot \pi \cdot f \cdot t) \qquad Eq. 3.31$$

where A is the amplitude of the wave, f is the frequency, and t is the time. The value of A from the mechanical approach is given by Eq. 3.19. The value of A from the geometrical approach is given by Eq. 3.30.

The maximum amplitude, A, of the mechanical model as a cantilever was approximately 287 mV. The maximum amplitude of the geometrical model was approximately 263 mV. The frequency for this example was set to 25 Hz. The signal was sampled for 655.36 ms. The expected signal was projected to appear as Figure 16.

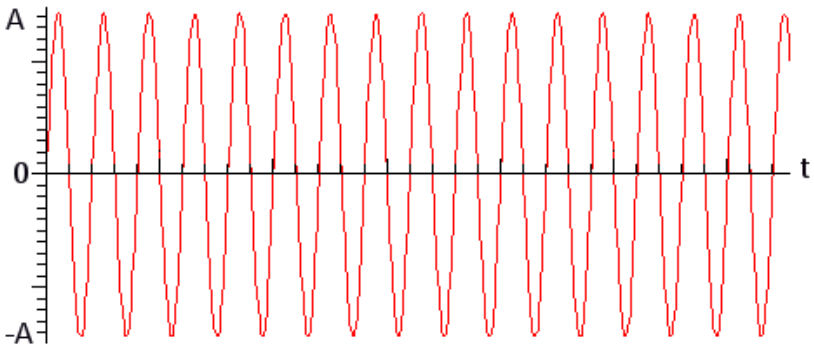


Figure 16: Expected time domain signal

Failure mode indications in the time domain were observed when the signal did not follow this sinusoidal shape and amplitudes were smaller or larger than expected.

3.4.2. The amplitude domain

A histogram of a signal tells how often the signal attains a particular value [32]. A sinusoidal signal output oscillates between two peaks. Visually, when the slope of the signal is small, the signal spends a long time at that value. When the slope is large, the signal spends very little time there. The histogram of a normal strain gauge is expected to appear as a U-shaped distribution, centered about zero. Mathematically, this was confirmed by examining an ideal sinusoid, given by:

$$y = A \cdot \sin(x) \qquad Eq.\,3.32$$

This is a representation of the expected signal from the strain gauge measurements on the oscilloscope. The slope of the sin wave is the derivative, given by:

$$\frac{dy}{dx} = \mathrm{A} \cdot \cos(x) \qquad Eq.\,3.33$$

Eq. 3.33 can be modified with trigonometry to

$$\frac{dy}{dx} = A \cdot \sqrt{1 - \sin(x)^2} \qquad \mathrm{Eq.}\,3.34$$

Remembering Eq. 3.32, this can then be modified to

$$\frac{dy}{dx} = \sqrt{A^2 - y^2} \qquad Eq.\,3.35$$

The amount of time, x, that a function spends around a value, y, is inversely proportional to the rate of change, $\frac{dy}{dx}$ [32]. Thus, the histogram is the reciprocal of the derivative, given by:

$$\frac{dx}{dy} = \frac{1}{\sqrt{A^2 - y^2}} \qquad Eq.\,3.36$$

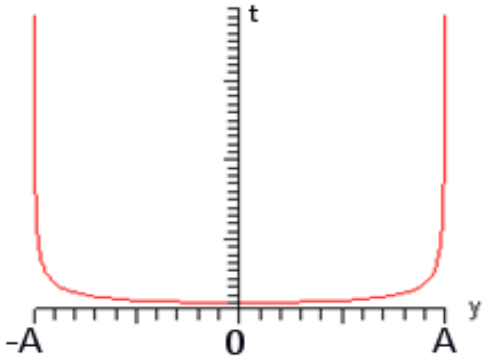


Figure 17: Histogram as a U-shaped distribution

This is an example U-shaped distribution that is centered about zero. Figure 17 shows an example of this distribution for an ideal sinusoid of amplitude, A. Failure mode indications in the amplitude domain were observed when the signal did not follow this U-shaped distribution.

3.4.3. The frequency domain

When observing an infinite continuous-time sine wave, x(t), the frequency domain of the signal appears as two impulses located at the fundamental frequency. However, the actual spectrum of sampled data is found as a discrete Fourier transform over a finite time interval, T.

Applying a rectangular window to an infinite sine wave limits the existence of the wave to the time interval, T. Figure 18 illustrates a window function applied to an infinite sine wave to limit it to a time, T.

The spectrum of the window function, w(t), appears as a main lobe with several decreasing side lobes. The spectrum of the time-limited sine wave, y(t) is the convolution of x(t) and w(t). The spectrum of the windowed sine wave, y(t), is similar to Figure 19 A, with primary lobes at the fundamental frequency and tapering side lobes [33].

The frequency analysis of the sampled signal, y(n), was expected to generate a large concentration about the fundamental frequency, with other noise spread out throughout the spectrum, as shown in Figure 19 B [33].

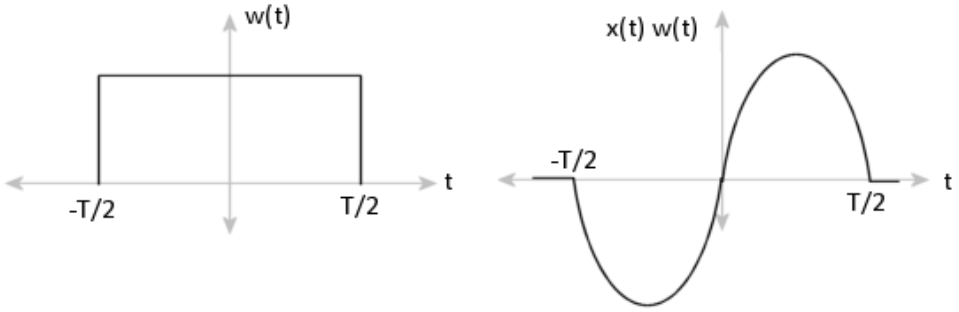


Figure 18: Window function and time limited sine wave

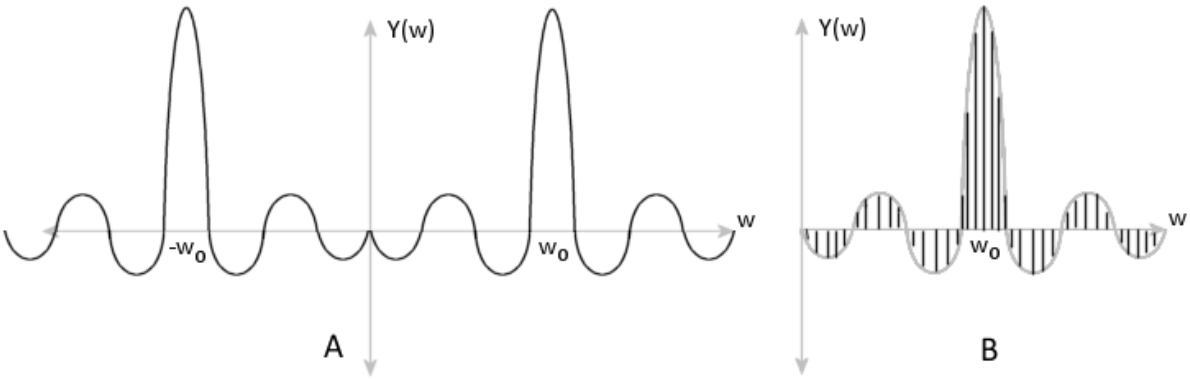


Figure 19: Spectrum of windowed sine wave (A) and sampled spectrum of finite length sine wave (B)

Failure mode indications in the frequency domain were observed when harmonics were apparent with the fundamental frequency or when the measured frequency did not match the driving frequency.

3.5. The experimental results

Several experiments were conducted by bonding strain gauges to the beam and subjecting the beam to different vertical displacements at different frequencies, by the methods outlined in this thesis. Results were obtained and stored in a database and analyzed to understand the relationship between the theoretical models and the experimental results. The data analysis software generated plots in the time, amplitude, and frequency domain. Those theoretical plots and values were quantitatively and qualitatively compared to the actual experimental results generated in the laboratory.

3.5.1. The time domain

The beam was subjected to vertical displacements of ±2 mm, ±1.5 mm, ±1 mm, and ±0.5 mm, which were set at the caliper located 100 mm away from the aluminum block, at several different frequencies. The strain gauge on the beam experienced a particular range of strains dependant on the vertical displacement. Figures 20-23 show the voltages measured by the data acquisition system versus the theoretical voltages developed for the electro-mechanical driving system at a frequency of 25 Hz.

The measured results were confirmed to have the same sinusoidal shape as predicted by the theoretical model; however, the measured signal had a smaller amplitude than that of the model. When the vertical displacement, δ_x, was 1 mm, the theoretical model showed a peak-to-peak voltage of 572 mV. In the actual experimental results at 1 mm, the measured signal showed a peak-to-peak voltage of approximately 332.813 mV. A correction factor of 0.5818 was applied to the theoretical signal to match the experimental signal.

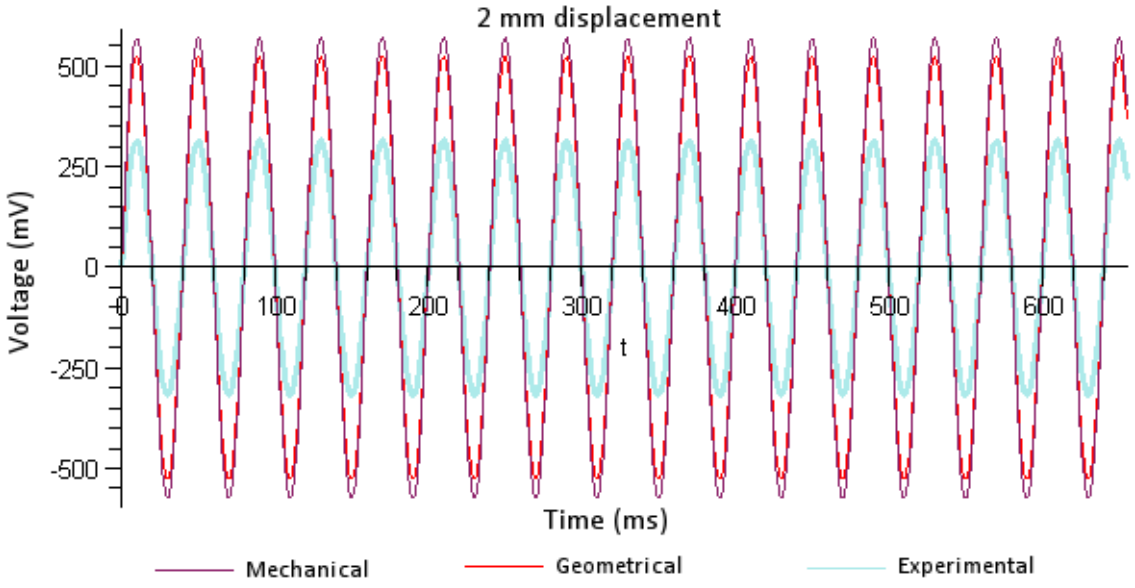


Figure 20: 2 mm displacement

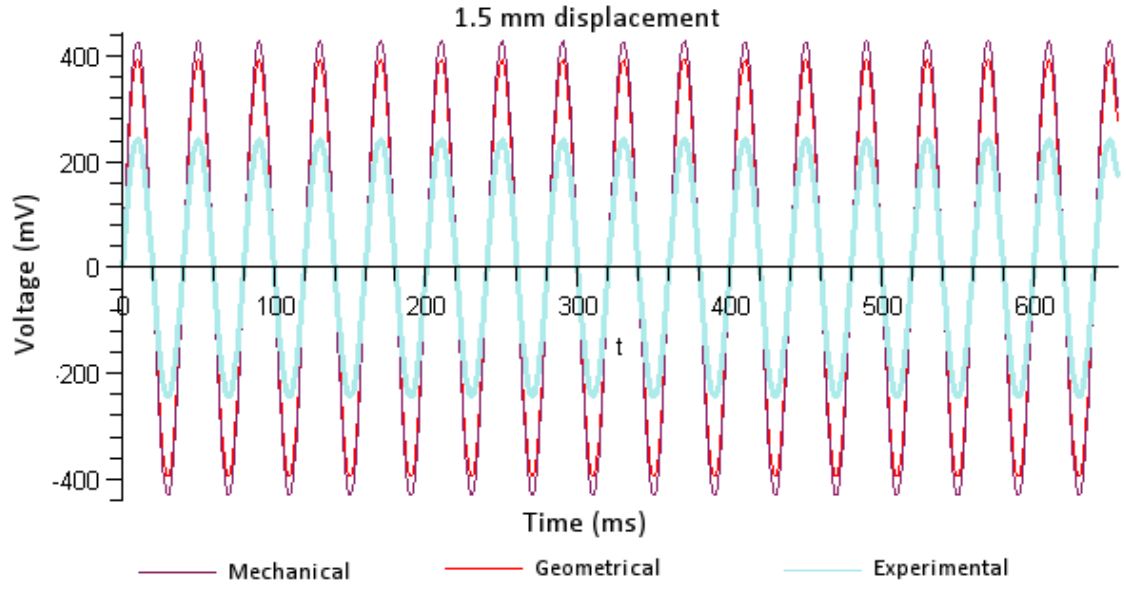


Figure 21: 1.5 mm displacement

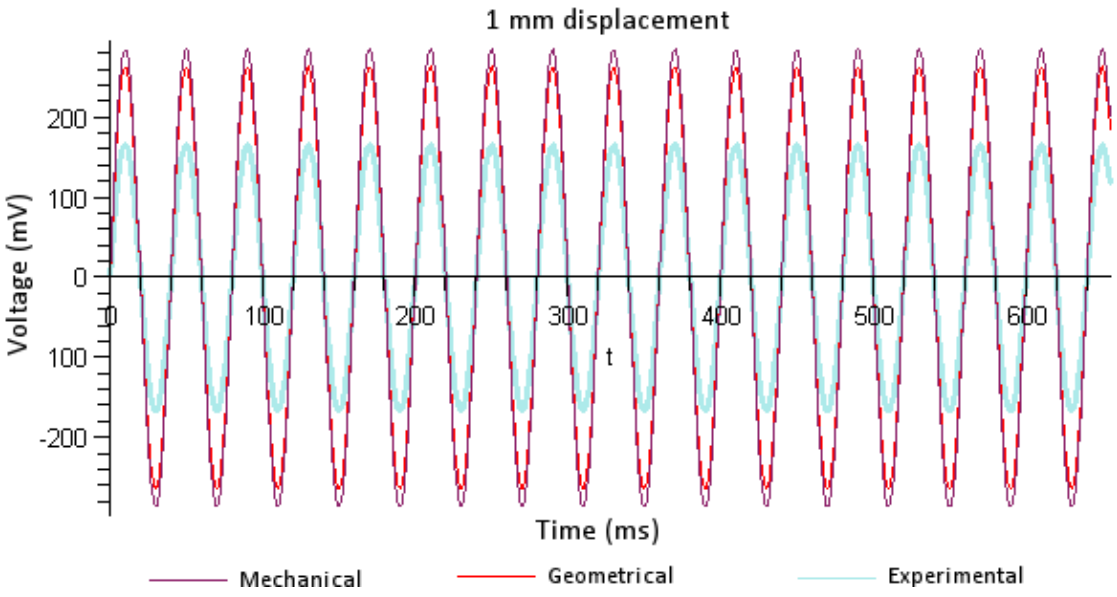


Figure 22: 1 mm displacement

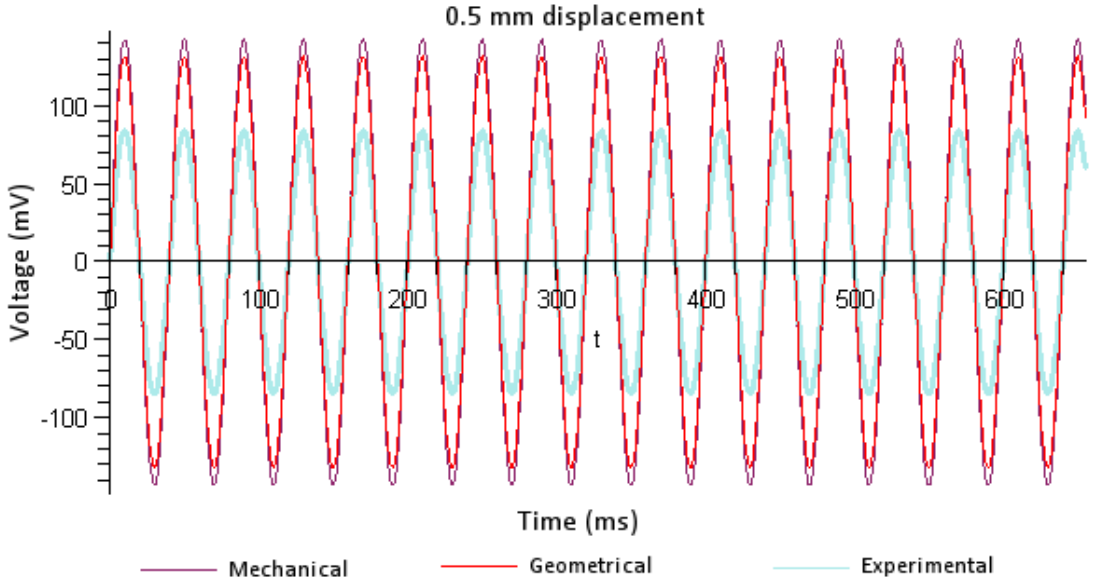


Figure 23: 0.5 mm displacement

In fact, all of the theoretical results, developed from the mechanical model, were required to have a correction factor to relate them to the measured experimental voltage from the laboratory. The correction factor for each experiment was approximately equal depending on the vertical displacement. Table 4 gives the specific percentage differences between 0.5 mm and 2 mm of vertical deflection for the average of the several measured results.

Figure 24 is an approximately linear relationship of the correction factor that is applied to the testing station to relate the theoretical results and the experimental results. These correction factors were roughly true for each experiment at the indicated displacements. Applying these correction factors to the theoretical models yielded results approximately equal to the measured signals.

Table 4: Correction factor from an example set of data with different vertical displacements

Vertical Displacement (mm)	Mechanical peak-to-peak voltage (mV)	Geometrical peak-to-peak voltage (mV)	Measured peak-to-peak voltage (mV)	Mechanical Percentage Difference (%)
2.0 mm	1146	1052	632.813	55.22%
1.5 mm	860	789	487.5	56.69%
1.0 mm	572	526	332.813	58.18%
0.5 mm	286	263	168.75	59.00%

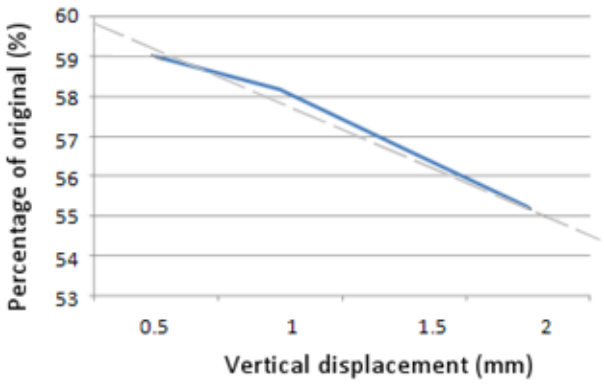


Figure 24: Experimental correction factor

While the measured signals do in fact confirm the theoretical sinusoidal shape, several speculations were made to explain the differences between amplitudes of the theoretical and measured signals.

1) The equations from the mechanical model are, at best, approximately true. The beam bending analysis was based on ideal material properties and boundary conditions. The actual testing station and mechanical motion are not ideal. Tabulated values were used to account for the material properties and bending of the beam. The aluminum beam itself was reused from a previous static experiment and may not have ideally bent as expected. The mechanical model assumed that the bending occurred about the center of the beam. It also assumed that the slope point where the loudspeaker connected to the beam was zero.
2) The geometrical approach assumed that the beam bending occurred in a perfect circular arc, disregarding material properties and loading. In any application of beam bending, it is essential to account for these circumstances. The values were approximations of the lengths of a bending beam.
3) Experimentally, measurement of the displacement was measured by sight and sound at the location of the caliper. These measurements were conservative. The audio amplifier also often drove the loudspeaker quite rigorously. At times, the motion of the beam may have been affected by the driving of the loudspeaker. The station was only tested at low amplitudes.
4) Bonding the strain gauge to the surface of the aluminum beam may have affected the material properties of the beam.
5) The experimental results relied more on reproducibility than precision. Measurements of failure modes were compared against measurements of control cases. In fact, [29] states that it is not always necessary to have exact values of strain in every application. The models were developed to understand what should be happening with strain from the mechanical motion. While the basic forms of each domain were confirmed, further analysis is required to understand all of the discrepancies between the theoretical models and experimental results.

3.5.2. The amplitude domain

The amplitude domain was expected to have a U-shaped distribution between the maximum and minimum amplitude centered about the time axis, illustrated in Figure 25. The histogram was found by applying the algorithm in Appendix E to the discrete values of the time domain. The resulting signal shows how often the time-domain signal

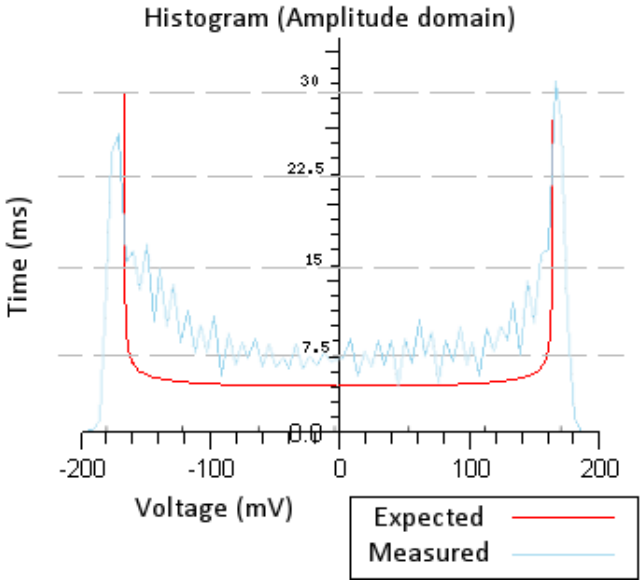


Figure 25: Measured amplitude domain versus

attains a particular amplitude. The experimental amplitude domain was confirmed to match the expected shape. Each strain gauge operating in a non-failure mode generated a histogram that resembled Figure 25.

3.5.3. The frequency domain

The frequency domain was expected to have a large concentration at the location of the fundamental frequency. The actual discrete-time Fourier transform, calculated by following the algorithm in Appendix E, confirms the presence of the spike at the proper frequency. Each strain gauge operating in a non-failure mode generated a corresponding spike at the correct fundamental frequency. For this particular example, the spike was found at 25 Hz, the frequency generated by the signal generator. This matches the expected frequency domain signal shown in Figure 26.

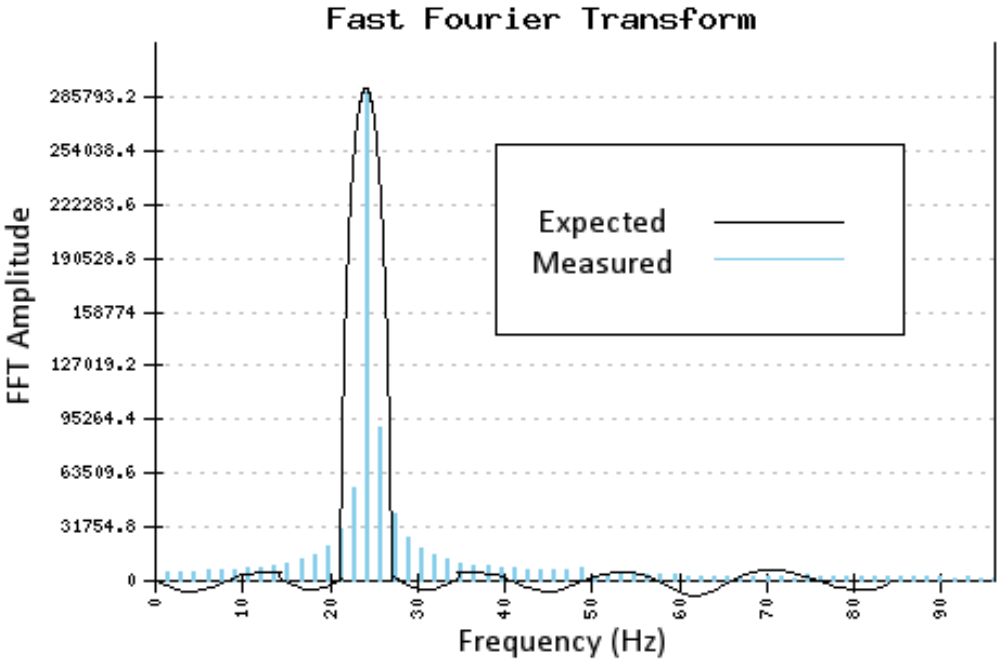


Figure 26: Measured frequency domain versus theoretical frequency domain

CHAPTER IV
MODELING AND EXPERIMENTAL ANALYSIS OF FAILURE MODES

4.1. Failure modes

The results presented in the Section 3.5 represent the expected cases for strain gauge testing in the time, amplitude, and frequency domain operating in non-failure situations. When operating in failure situations, the strain gauge signals deviated from the models developed in the previous chapter. A failure mode is a situation in which a sensor fails to meet its design characteristics [9]. A failure mode of a strain gauge is a situation that causes the gauge to improperly measure the strain and thus not generate the expected results. Some potential failure modes of strain gauges include [34]:

1) Improper gauge installation
2) Over-straining
3) Operating outside the temperature limits
4) Physical damage and environmental wear
5) Improper gauge selection

Improper gauge installation can cause a strain gauge to generate undesirable results. In general, strain gauges are guaranteed operational out of the package. Problems with the signal are the fault of the user or some mechanical error. The techniques provided by vendors are tested to ensure the best possible bond and solder connection. Surface conditions are required to be smooth and clean. Adhesives are also required to be fresh. Small errors in installation can cause drastic deviations in the measured results [35].

Over-straining is pushing the strain gauge beyond its operational limits. Excessive loading can exceed the maximum detection abilities of a strain gauge to measure strain on a surface. The resulting measured strain can be erroneous. If the surface elongation extends beyond the capability of the strain gauge, the gauge may be physically damaged beyond repair.

Each strain gauge is rated to operate within a given temperature range. Some strain gauges may operate outside of that range for short periods of time. The Vishay® EA-06-062AP-120 strain gauge is rated to operate normally between -100˚ and 350˚F, or

between -320˚ and 400˚F for a short period of time [13]. Operating outside of these temperature ranges can yield failure results.

Physical damage can alter the fundamental operation of a strain gauge, discussed in Chapter 2. If part of the grid is damaged, the gauge may not correctly detect the strain on the surface of the beam. Environmental wear can lead to physical damage, corrosion, grid deformation, or cracking [9].

While improper gauge selection is not a physical failure mode, it can cause strain measurements to be read incorrectly, which is the definition of a failure mode in this literature. There are several different kinds of strain gauges, with different grid alignments. This research focuses on axial strain longitudinally along the beam. Figure 27 shows several different strain gauge grid alignments available from Vishay® [36]. The first gauge was selected to measure axial strain.

Strain gauges are quite reliable if proper care is taken during installation and operation. Vendors pay special attention to the manufacturing and inspection of strain gauges to ensure quality control. Properly installed strain gauges can survive almost any situation short of total surface failure beneath the gauge [35]. Because of the quality control of strain gauges, many difficulties were encountered in producing failure modes in a laboratory environment. Some potential failure modes, such as over-strain and temperature effects, were beyond the experimental scope of the testing station. The small nature of the sensor and the strength of the bonding materials caused much difficulty in generating failure characteristics during gauge installation.

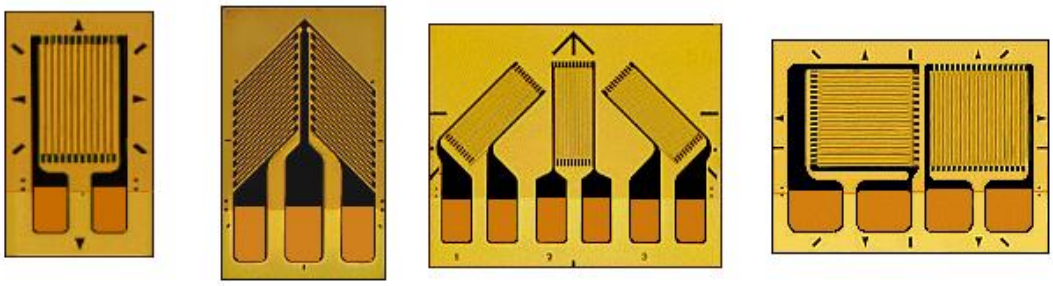


Figure 27: Vishay® strain gauge grid alignments

This research study was the introductory phase of an investigation of strain gauge failure modes. The analysis of failure modes began by addressing two such situations arising from gauge installation. Debonding can occur if a strain gauge is not properly bonded following techniques such as the one outlined in Appendix A. Lead termination can occur is the wire leads are not properly soldered following techniques such as the one outlined in Appendix B. These two situations were modeled and analyzed in the strain gauge testing station.

4.2. Debonding model

Bonding is the process of attaching a strain gauge to a surface. Debonding in this literature is defined as the process of the strain gauge becoming unattached from the surface, or the separation of bonded surfaces [37]. Debonding occurred by several means, including:

1) Peeling a strain gauge from the surface
2) Gradual weakening of the bond over time
3) Improper bonding during gauge installation

To understand some of the syndromes of debonding occurring on the strain gauge testing station, this model was developed to relate the amount of strain, resistance measured by the strain gauge, and the ratio of bonded area to total area. This is illustrated in Figure 28.

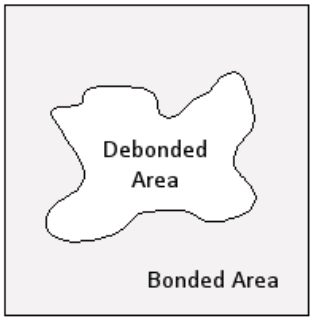


Figure 28: Ratio of debonded area to bonded area of grid

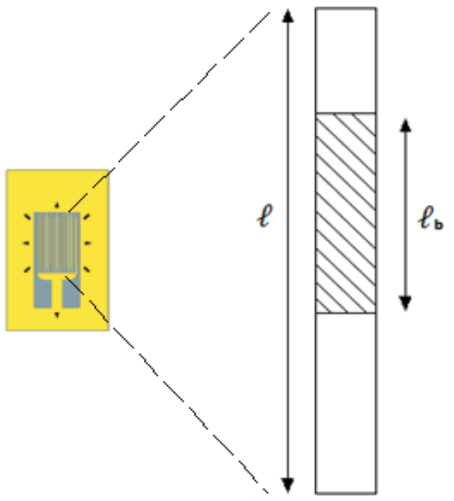


Figure 29: Ratio of bonded length to debonded length

4.2.1. Debonding model and theory

The following model was developed under three assumptions.

1) Change in resistivity of the wire is minimal because of the constantan material
2) Change in cross-sectional area is minimal
3) Strain on the surface is uniform over the small area of the gauge

The EA-06-062AP-120 strain gauge active grid consists of 16 legs that run longitudinally between the end caps. Each leg, of length ℓ, of the strain gauge grid has a distance of fully bonded length, ℓ_b. Figure 29 illustrates a portion of a leg that is bonded and another portion that is debonded.

The portion of the wire that is fully bonded experiences the full elongation of the surface from the fundamental definition of the resistance of a wire, given by:

$$R_b = \frac{\rho \cdot \ell_b}{w \cdot h} \qquad Eq.4.1$$

The resistance of the i^{th} strained leg is the summation of the resistance of the length of wire that is completely debonded, the resistance of the wire that is fully bonded, and the change in resistance resulting from the elongation of the surface on the fully bonded section.

$$R_i = \frac{\rho \cdot (\ell - \ell_b)}{w \cdot h} + \frac{\rho \cdot \ell_b}{w \cdot h} + dR_b \qquad Eq.4.2$$

where dR_b is the resistance change of the length of fully bonded wire, caused by the axial strain, ε_ℓ. The first two terms of Eq. 4.2 are the total resistance of a leg of the unstrained wire. Therefore, as expected, the resistance of a leg is its unstrained resistance plus a change in resistance cause by strain:

$$R_i = R + dR_b \qquad Eq.4.3$$

Assuming that the strain is uniform over the small area, the resistance change, dR_b, is given by:

$$dR_b = R_b \cdot \varepsilon_\ell \cdot GF \qquad Eq.4.4$$

Using Eq. 4.4, Eq. 2.4, and multiplying by a factor of ℓ/ℓ, the change in bonded resistance is:

$$dR_b = dR \cdot \left(\frac{\ell_b}{\ell}\right) \qquad Eq.4.5$$

where dR is the change in resistance of a fully bonded wire. Substituting this back into Eq. 4.3 gives:

$$R_i = R + dR \cdot \left(\frac{\ell_b}{\ell}\right) \qquad Eq.4.6$$

R is the resistance of the wire experiencing no strain. The strained resistance of a wire, R_i, can be determined as a percentage of the length of the wire fully bonded to the total length of the wire. The total resistance over the entire gauge is the summation of the resistances of N number of legs.

$$R_{total} = \sum_{i=1}^{N} R_i \qquad Eq.4.7$$

A ratio of bonded length to total length, L_i, for a particular leg is given by:

$$L_i = \frac{\ell_b}{\ell} \qquad Eq.4.8$$

Combining Eq. 4.6, 4.7, and 4.8 gives:

$$R_{total} = N \cdot R + (N \cdot dR) \cdot \left(\frac{1}{N} \cdot \sum_{i=1}^{N} L_i\right) \qquad Eq.4.9$$

Multiplying by a width ratio and assuming that the change in cross sectional area is minimal, the length ratio from Eq. 4.19 is written in terms of the ratio of bonded area to total area.

$$\left(\frac{1}{N} \cdot \sum_{i=1}^{N} \frac{\ell_b}{\ell}\right) \cdot \left(\frac{width\ of\ wire}{width\ of\ wire}\right) = \frac{A_{bonded}}{A_{total}} \qquad Eq.4.10$$

Recalling that the total resistance of an unstrained grid, $R_{total\ _unstrained}$, is $N \cdot R$ and the total change in resistance, $dR_{total\ _strained}$, of a fully bonded grid is $N \cdot dR$, the total resistance is given by:

$$R_{total} = R_{total\ _unstrained} + dR_{total\ _strained} \cdot \left(\frac{A_{bonded}}{A_{total}}\right) \qquad Eq.4.11$$

The value, $R_{total\ _unstrained}$, is nominal resistance of the strain gauge. The value, $R_{total\ _strained}$, is the total change of resistance if the gauge were fully bonded to the surface. Eq. 4.11 gives the total resistance of the strain gauge in terms of the nominal resistance, the total change in resistance during an applied strain, and the ratio of bonded area to total area.

4.2.2. Example situations

When the strain gauge is fully bonded, a typical signal under tension and compression in the time domain is shown in Figure 30. In this situation, the strain gauge experiences all of the elongation of the beam, and, in theory, generates an equal and opposite amplitude, A, for tension and compression.

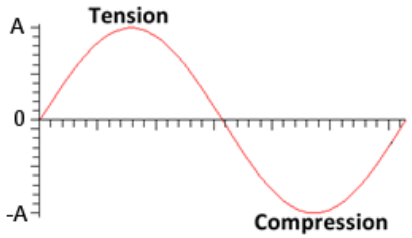


Figure 30: Example signal of tension and compression

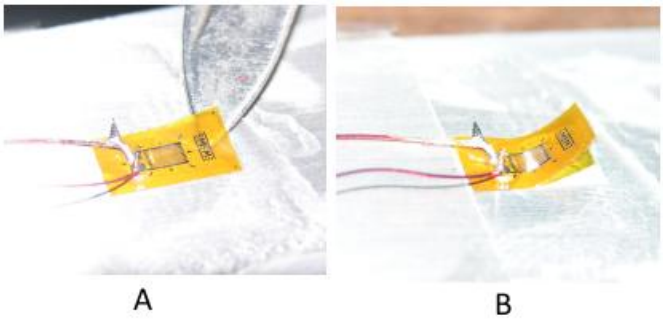


Figure 31: Peeling a gauge from the surface (A) and partial grid attachment (B)

As portions of the strain gauge grid become debonded, the signal experiences a loss in amplitude from the ratio of bonded area to bonded area in Eq. 4.14. A fully bonded area is unity and experiences all of the elongation of the surface. As the bonded area decreases, the ratio decreases, causing a proportional amount of the resistance change to contribute to the total resistance. Figure 31 shows an example of peeling the strain gauge from the surface, decreasing the area of the grid that is experiencing the full elongation.

From the example for the derivation of the cantilever in Section 3.2, the output voltage was calculated as ±287 mV. The nominal resistance R was 120Ω and the change in resistance of the gauge was 0.08Ω. Using these values, Eq. 4.11, and the Wheatstone bridge equation, a means of calculating the voltage in terms of the percentage of bonded area, P, is given by:

$$V_{out} = 3.3 \cdot \left[\frac{R + dR \cdot P}{R + dR \cdot P + 120} - \frac{1}{2}\right] \cdot 522 \cdot 1000 \qquad Eq. 4.12$$

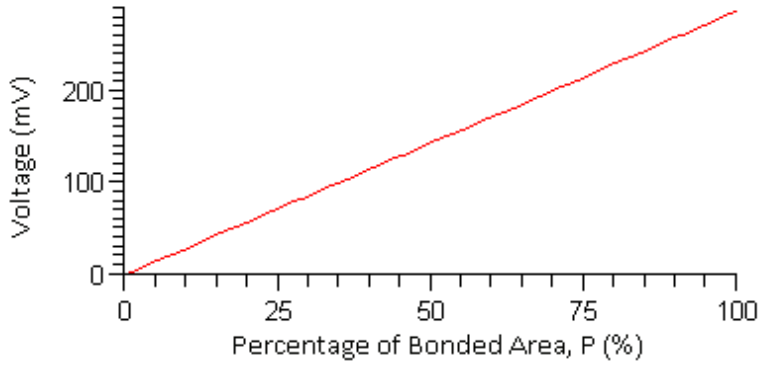


Figure 32: Output voltage as a function of percentage of bonded area

where $0 < P < 1$. Figure 32 shows that this relationship is linear with respect to the percentage of area that is bonded. For example, when P is 50%, the strain gauge grid experiences half of the surface elongation, $dR \cdot P$, and the output voltage is approximately 143.5 mV, half of the expected 287 mV.

Some deformation of the signal can also occur when regions of the gauge become debonded. If a horizontal slice across the middle of the strain gauge grid debonds, while the top and bottom portions of the gauge remain bonded, the gauge may not be affected by the elongation at all times. During tension, the grid may be pulled tight enough against the surface to fully transfer all of the elongation characteristics; however during compression, the grid may not be fully connected to the beam. This causes asymmetry in the output signal amplitude. During tension, the strain gauge measures the full elongation of the surface. During compression, the strain gauge measures only a percentage of the elongation. This signal continues throughout the process of acquiring data. This process and its associated syndrome are illustrated in Figure 33.

4.2.3. Debonding results

Several experiments were conducted to observe the effects of peeling the strain gauge from the surface to change the size of the bonded area. The results of this test are shown in Figure 34 and Table 5. In each experiment, the signal gradually decreased in amplitude until signal termination occurred, or the gauge was completely removed from the surface. In this particular setting, the station was set to 25 Hz with a vertical displacement of 2 mm at the caliper. The original signal had a

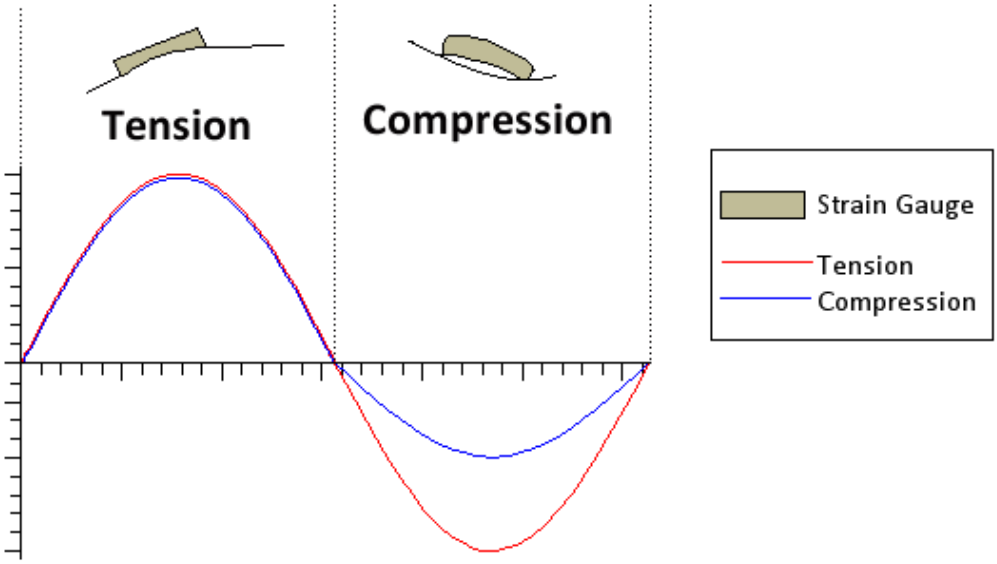


Figure 33: Non-symmetric detection during tension and compression

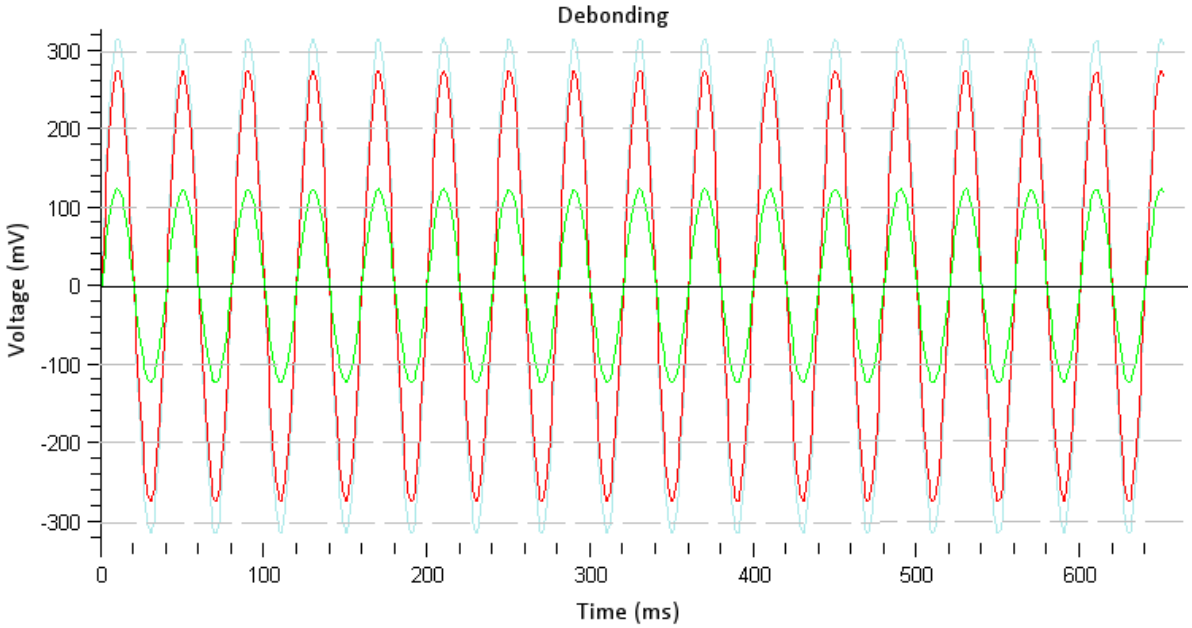


Figure 34: Signal decrease in amplitude during debonding

Table 5: Measured decrease in amplitude during debonding

Maximum Value (mV)	Minimum Value (mV)	Measured Percentage of Original (%)
309.375	-323.438	100%
271.875	-278.395	86.96%
121.475	-125.822	39.08%

peak-to-peak voltage of 632.813 mV. In the subsequent tests, the peak-to-peak voltage decreased in size by a particular percentage. Although visual inspection verified that debonding occurred, no estimations were accurately made predicting the actual ratio of bonded area to total area.

Some of the experiments showed signal deformation attributed to debonding in the interior part of the strain gauge as discussed in the previous section. Figure 35 shows the results of one such experiment. The tensile stage of the signal appeared to be fully transmitted. On the other hand, the compressive stage of the signal was much smaller in amplitude. The maximum voltage displays approximately 75 mV during tension, while the minimum voltage is approximately -35 mV during compression.

4.3. Lead termination model

Lead termination in this literature is defined as the point at which the wire lead becomes disconnected from the solder bead on the strain gauge. Of particular interest was observing results when the lead was becoming disconnected, but had not yet fully detached from the gauge. Lead termination occurred by several means, including:

1) Pulling or loosening the wire by physical force
2) Weakening of the solder connection over time
3) Improper soldering during gauge installation

To understand the output signal that resulted from this situation, the strain gauge and the solder bead resistance were modeled as random variable resistors. Resistors are summed when arranged in series and their probability density functions are convolved together [38].

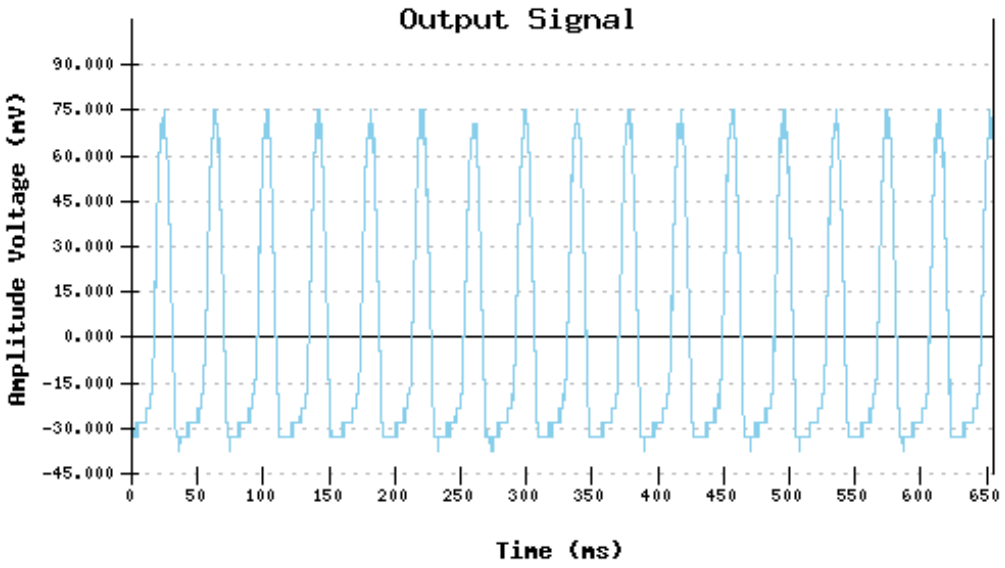


Figure 35: Signal from strain gauge showing non-symmetric detection during tension and compression because of interior debonding

4.3.1. Lead termination model and theory

A random variable, X, represents the voltage across the strain gauge, disregarding the DC component. The expected voltage signal is a sinusoid, given by:

$$X = A_o \cdot \sin(\theta) \qquad Eq.4.13$$

where θ is uniform on (-π, π). The PDF of X, derived in Section 3.4.2, is a U-shaped distribution between $-A_o$ and A_o, determined in Chapter 3. The PDF is given by:

$$p_X(x) = \frac{1}{\sqrt{A_o^2 - x^2}} \quad for\ |x| \leq A_o \qquad Eq.4.14$$

Another random variable, Y, is the voltage across the lead connection on the solder tab of the strain gauge. It is difficult to model an unknown varying resistance. Models must be developed around assumptions. Resistance is always non-negative and has a positive distribution. Therefore, one such approach for examining the initial stages of lead termination assumes the PDF of this random variable takes the form of a one-sided exponential. This is given by:

$$p_Y(y) = \frac{1}{V_o} \cdot e^{-y/V_o} \cdot u(y) \qquad Eq.4.15$$

A random variable, Z, represents the sum of X and Y. Therefore, the PDF of Z is the convolution of the PDF's of X and Y, given by:

$$p_Z(z) = \int_{-\infty}^{\infty} p_X(x) \cdot p_Y(z - x) \cdot dx \qquad Eq.4.16$$

Substituting in the PDF's for X and Y gives the PDF of Z.

$$p_Z(z) = \frac{e^{-z/V_o}}{V_O} \int_{-A_o}^{A_o} \frac{e^{x/V_o}}{\sqrt{A_O^2 - x^2}} \cdot u(z - x) \cdot dx \qquad Eq.4.17$$

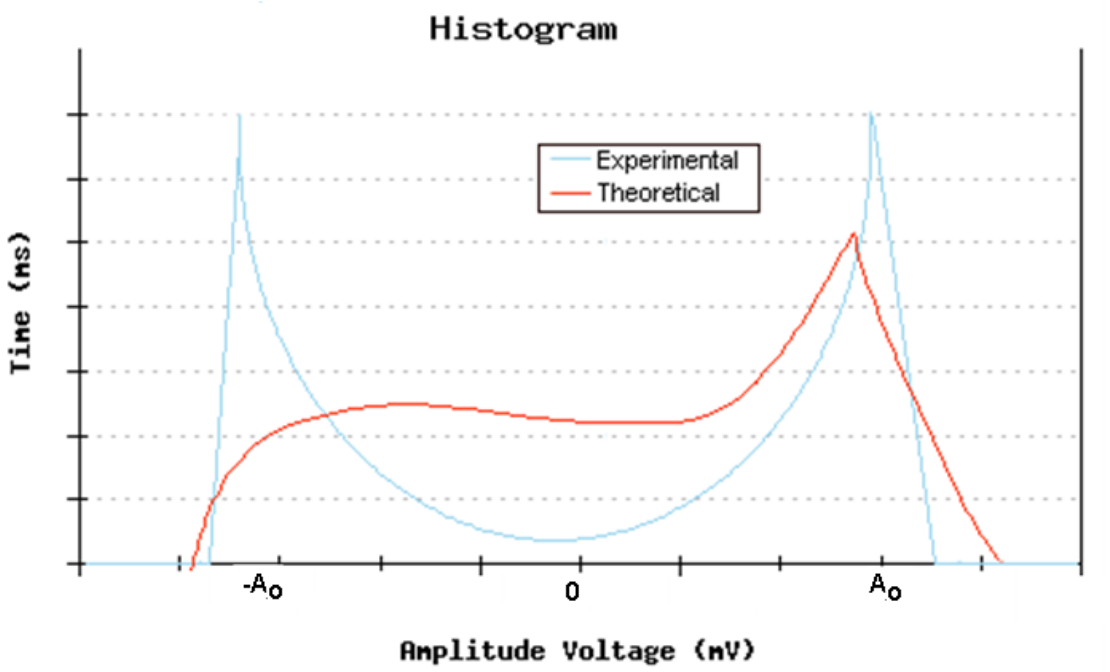


Figure 36: Theoretical model versus expected experimental results

Visually, this is the convolution of an exponential and a U-shaped distribution, illustrated in Figure 36. The ideal lead histogram is the U-shaped distribution. The theoretical loose lead amplitude domain contains a peak at the maximum value. However, the peak at the minimum value is absent.

Numerically convolving, for $z < -A_o$,

$$p_Z(z) = 0 \qquad Eq.\,4.21$$

For $-A_o < z < A_o$:

$$p_Z(z) = \frac{e^{-z/V_o}}{V_O} \int_{-A_o}^{z} \frac{e^{x/V_o}}{\sqrt{A_O^2 - x^2}} \cdot dx \qquad Eq.\,4.22$$

For $z > A_o$:

$$p_Z(z) = e^{-z/V_o} \cdot \left\{ \frac{1}{V_o} \cdot \int_{-A_o}^{A_o} \frac{e^{x/V_o}}{\sqrt{A_o^2 - x^2}} \cdot dx \right\} \qquad Eq.\,4.23$$

In Eq. 4.23, the term in brackets is not a function of z, therefore, $p_Z(z)$ falls off as an exponential after $z > A_o$.

4.3.2. Example situation

Lead termination failure occurred when the lead was almost to the point of complete detachment from the solder bead. In this particular example, the lead was operating in the initial stages of termination. The solder bead on the left solder tab of the strain gauge began to wear away. The lead began to break through the solder bead during operation. In the right solder tab, the lead was secured into the solder bead with a good connection.

It was not observed how this particular lead termination, shown in Figure 37, occurred; however possible causes include improperly soldering the lead into the solder bead during gauge installation or physical damage that caused the solder to wear away at the location of the lead.

4.3.3. Lead termination results

This particular example of lead termination occurred when the signal generator was set at 25 Hz but at a smaller gain than in the normal operation examples shown in Chapter 3. In the time-domain, the signal appears to experience the tension normally, but during compression, the signal appears smaller in amplitude and inverted. The wire appeared to have a complete connection with the solder bead during tension; however, during compression, the wire became loose and began to terminate from the bead.

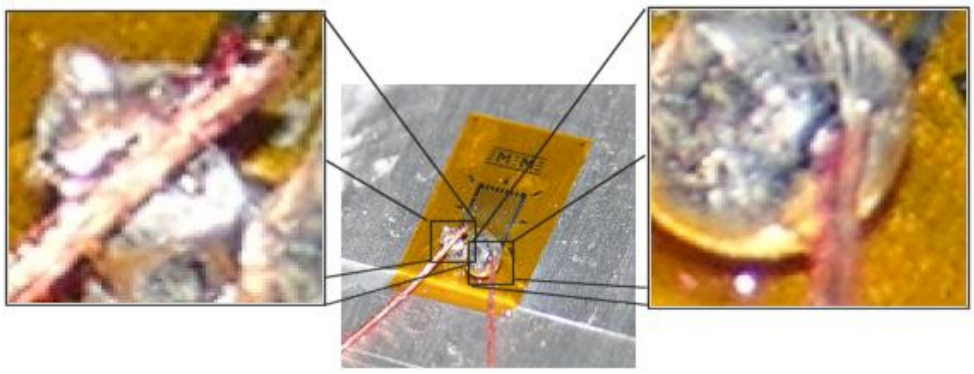


Figure 37: Lead termination example: left lead terminating, right lead secure

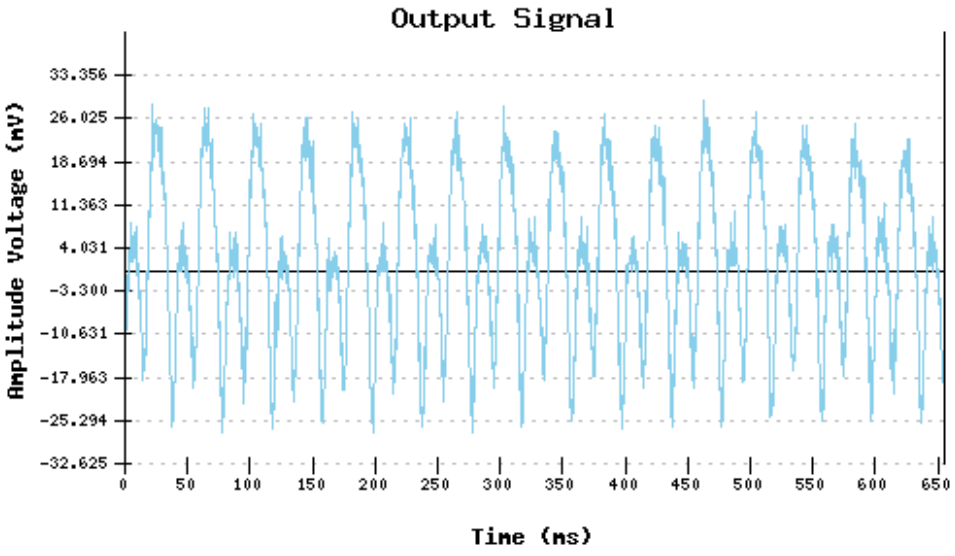


Figure 38: Signal of strain gauge because of lead termination

During the initial stages of lead termination, the measured signal was shown below in Figure 38. This form of the signal was measured from several strain gauges tested for lead termination.

The histogram of the strain gauge undergoing lead termination did not appear as the expected U-shaped distribution. Instead, it appeared similar to the theoretical model derived in Section 4.3.1. The histogram is shown in Figure 39.

However, there was a discrepancy because of the simple model for lead resistance. The signal was complete during tension, but not during compression. The histogram peak is preserved at $+A_o$. The peak at $-A_o$ is absent, skewing the histogram toward positive voltages. Adjusting the A_o and V_o terms of the model to 25 mV and 5 mV respectively, the histogram of this signal is shown to have approximately the same form described by the theoretical model. The region of the signal during tension produces a peak approximately at 23 mV, while the region during tension produces a peak at approximately 8 mV. This generated a peak on the experimental results at the origin because it appeared more frequently than any other value in the signal. It appeared at the lower values less frequently, rolling off to the left of the histogram. A second peak occurred at the maximum value of the tension region.

Analyzing the spectrum of this signal revealed multiple harmonics of the fundamental frequency, 25 Hz. A larger amplitude appears at twice the fundamental frequency, 50

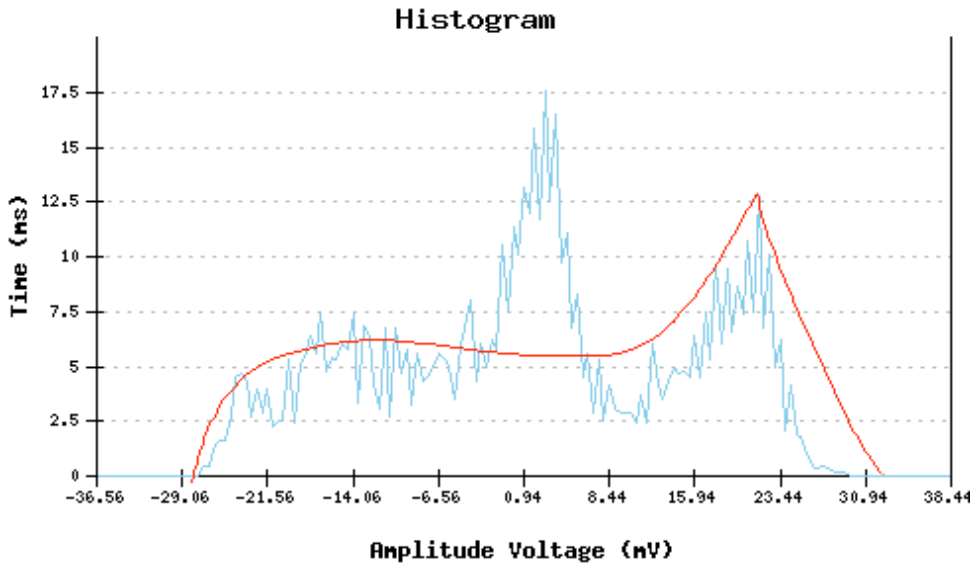


Figure 39: Comparison of theoretical and experimental amplitudes of strain gauges with wire lead termination

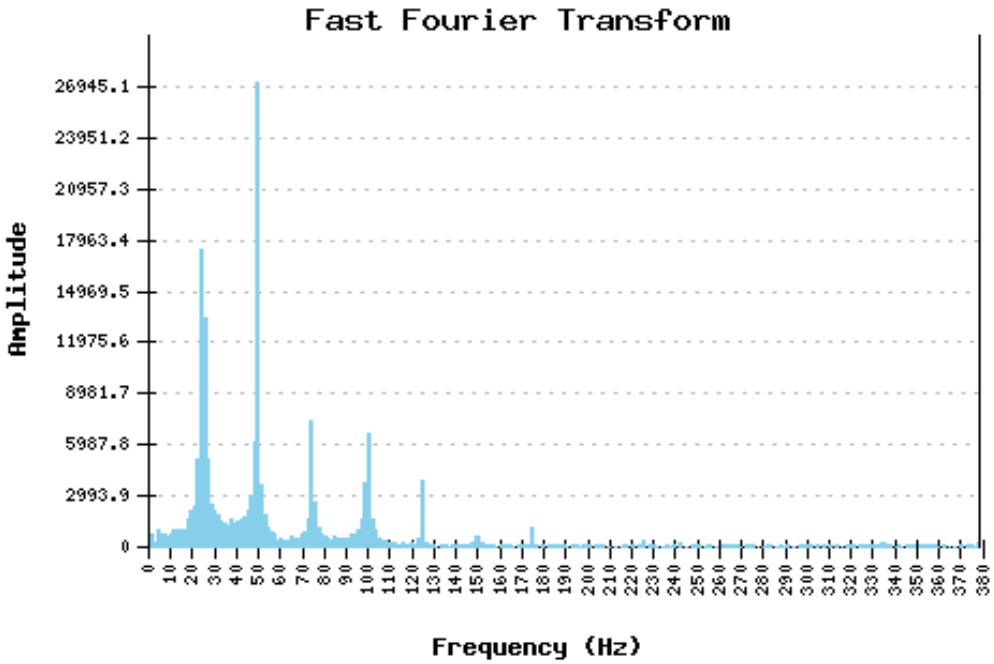


Figure 40: Frequency spectrum of lead termination example

Hz, because of the apparent doubling of the frequency evident in the time-domain. Large spikes are present at 75 Hz, 100 Hz, and 125 Hz and eventually taper off. The frequency domain of the lead termination failure mode is shown in Figure 40, between 0 and 380 Hz.

Additional signals were recorded at later stages of lead termination; however, no predictive models were determined to explain these erratic results. These signals are shown in Figures 41 and 42.

4.4. FMEA application

The models of debonding and lead termination were successfully verified during situations recreated in a laboratory environment. Lead termination showed loss in signal amplitude in one of the cases discussed. In another, it showed a non-symmetrical signal in which the tensile stage of the results was fully reported, but only a portion of the compressive stage was shown. The lead termination signal was determined to have a distribution mathematically predicted.

The results of the analysis were then used to generate an FMEA table to manage the failure modes. Failure mode descriptions, potential signal effects, potential causes of the failure, actions taken over the course of the research, and recommended actions to avoid similar circumstances are provided in this table. The models defined in the previous sections were included in the table as well as the potential failure modes discussed in the opening of this chapter. The FMEA form for this research is shown in Table 6.

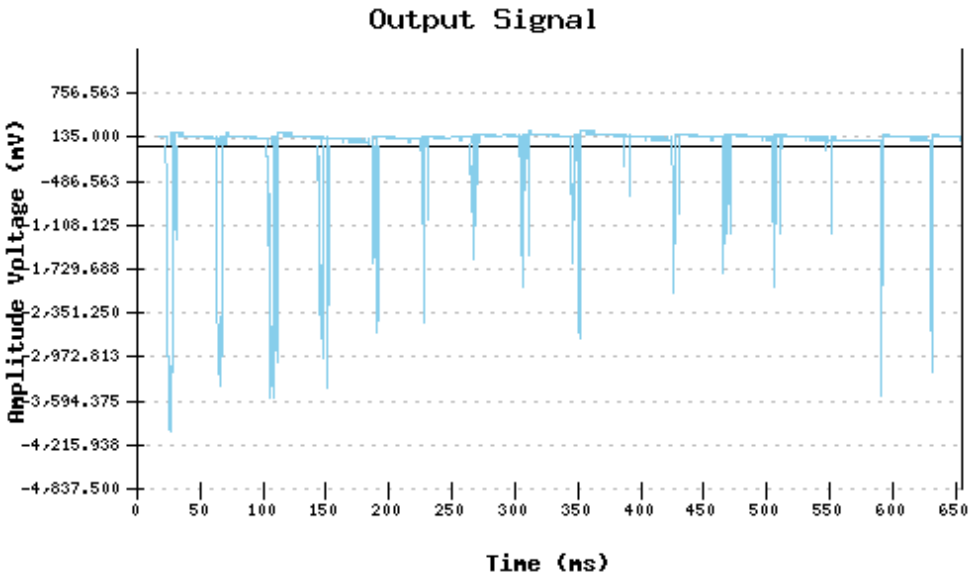


Figure 41: Strain gauge signals from later stages of lead termination (1)

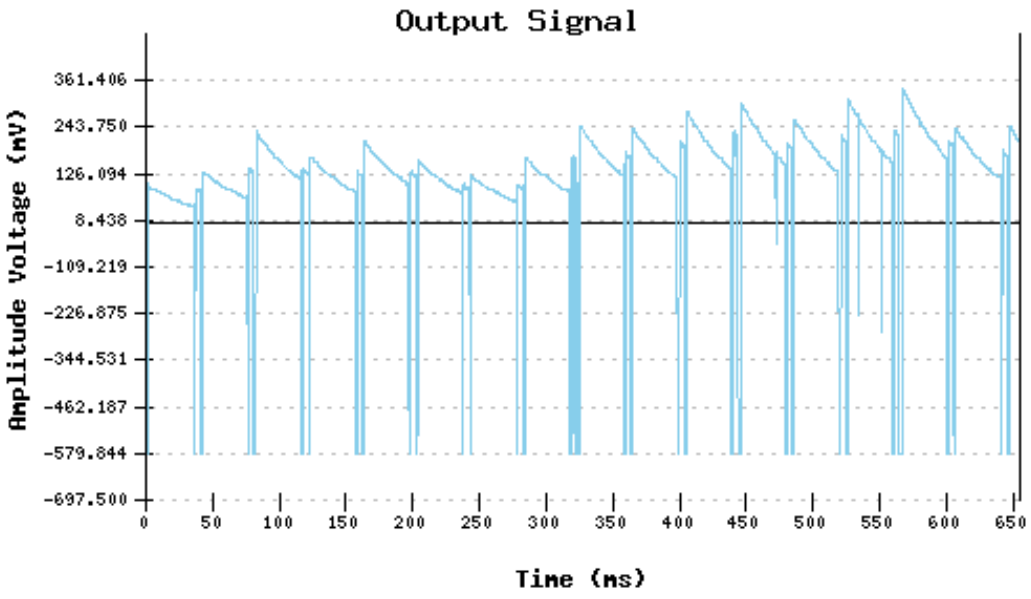


Figure 42: Strain gauge signals from later stages of lead termination (2)

Table 6: Documentation of FMEA for strain gauge testing

ID	Potential failure mode	Potential effects of failure modes of signals	Potential causes of failure modes	Actions taken	Recommended actions
0	None	None	None	1) Predictive models of the expected forms of signals in the time, amplitude, and frequency domain developed by analyzing strain gauges and classical beam bending analysis 2) Sample measurements obtained to verify the strain gauge testing station with corrective factors to account for deviations between model and experimental setup	1) Observe proper bonding and soldering techniques for successful gauge installation
1	Debonding	1) Loss of signal amplitude 2) Deformation of signal during compressive stage of signal	1) Peeling from surface 2) Gradual weakening of bond over time 3) Improper bonding techniques 4) Expired materials causing bond decay	1) Predictive model developed to show loss of amplitude in terms of the region of the grid bonded to surface 2) Predictive model developed to show example when region may not fully be attached during compression, but pulled tight during tension 3) Examples verified showing loss of signal amplitude and deformation during compressive stage.	1) Properly follow bonding techniques, such as Appendix A 2) Ensure that bonding materials have not expired
2	Lead termination	1) Signal deformation, compressive stage appears to be inverted with a smaller amplitude 2) Apparent doubling of fundamental frequency, with tapering harmonics of actual fundamental frequency 3) Amplitude domain appears as convolution of expected signal (U-shaped distribution) with an exponential signal	1) Pulling or loosening of wire by physical force 2) Weakening of lead connection over time 3) Improper soldering techniques	1) Predictive model developed to show the probability density function as the convolution of a U-shaped distribution and an exponential	1) Properly follow soldering techniques, such as Appendix B 2) Observe lead connections for decay or disconnection indications over course of experiment

Table 6: (Continued) Documentation of FMEA for strain gauge testing

ID	Potential failure mode	Potential effects of failure modes of signals	Potential causes of failure modes	Actions taken	Recommended actions
3	Over-strain	N/A	N/A	Theory introduced	Perform further testing in laboratory pushing strain gauge beyond operational limits
4	Thermal effects	N/A	N/A	Theory introduced	Perform further testing in laboratory during different heating and cooling environments
5	Physical damage or environmental wear	N/A	N/A	Theory introduced	Perform further testing in laboratory causing physical damage to the strain gauge
6	Improper gauge selection	N/A	N/A	1) Theory introduced 2) Example grid alignments examined	Perform further testing in laboratory by applying different strain gauges to the same situations and observing similarities and differences

CHAPTER V
CONCLUSIONS AND RECOMMENDATIONS

5.1. Conclusions

During stress testing of aircraft components, much research has been conducted to understand the process of component failure; however little research was available to understand strain gauge failure during cyclic operation. This introductory research was undertaken to define and prepare a strain gauge testing station for Failure Mode and Effects Analysis, and to verify its operation, experimentally. The work presented in this thesis provided an understanding of the mechanical motion of the testing station's beam bending analysis and the fundamental operation of strain gauges. It also showed examples of theoretical and experimental strain gauge failure modes. This was accomplished from the outset by following the steps outlined for FMEA testing.

The first objective was to gain a clear understanding the mechanical and electrical behavior of a typical, uniaxial strain gauge, as demonstrated in Chapter 2. This research examined the fundamental operation of the strain gauge and in particular, the Vishay® EA-06-062AP-120 strain gauge. The equations governing the operation of a strain gauge and the Wheatstone bridge measuring circuit were derived and applied to the predictive models of failure modes as discussed in Chapter 4. Proper bonding and soldering techniques were analyzed and determined to be potential causes of the failure modes discussed in Chapter 4.

The second objective was to understand the operation of the electro-mechanical driving system. After understanding how the deflections, stresses, and strains of the driven beam occurred, observing strain gauge failure modes was a matter of identifying the situations that deviated from the theoretical models. This was accomplished by applying classical beam bending analysis of a left-end-guided, right-end-fixed cantilever beam to the mechanical motion of the station. Predictive models were based on a mechanical theory and on a geometrical theory. Both approaches were developed and analyzed. Expected signal characteristics were determined to be a sinusoidal signal in the time domain, a U-shaped distribution in the amplitude domain, and a spike at fundamental frequency in the frequency domain. The experimental shapes of the measured strain gauge voltage signals were verified to be the same as the theoretical models; however, the amplitude of the experimental signals were found to be smaller

than predicted by the theoretical model. Some speculations were discussed as to why a correction factor was needed to equate the theoretical and expected measurements. Material properties, tabulated values, and approximations of equations were some of the theories for the differences. More work remains to be done to determine the exact causes of these differences.

The third objective was to generate block diagrams of each process. Appendix A illustrates the procedures performed in this research to bond a strain gauge to a testing surface. Appendix B shows the procedures performed in this research to solder the wire leads to the strain gauge solder tabs. Appendix D and Figure 7 illustrated the operation of the strain gauge testing station. Having a visual representation of each step made it easy to determine potential areas from which failure modes could arise.

The fourth objective was to develop a means of storing and analyzing the experimental results. A database was built to hold all of the measured results. This software was developed to observe the time, amplitude, and frequency domains, which were the domains of interest throughout this research. Algorithms, such as the histogram and discrete fast Fourier transform algorithms in Appendix E, were run to determine the amplitude and frequency domain plots of the signals. These algorithms allowed for qualitative and quantitative comparison of the theoretical models and experimental results.

The fifth objective was to identify potential failure modes and their causes. Two potential strain gauge failure modes, debonding and lead wire termination, were analyzed for FMEA documentation, shown in Chapter 4. Possible effects and causes were discussed for each of these situations. Other failure modes such as over-straining, improper temperature environment, physical damage, environmental wear, and improper gauge selection were mentioned, but not analyzed.

The final step was to observe, describe, and report the effects of the two failure modes. In particular, two particular failure modes were analyzed in regards to proper bonding and soldering techniques. Debonding of a strain gauge occurred when the strain gauge began to detach from the testing surface. Debonding was primarily evident in the time-domain as either a loss in amplitude or non-symmetric signal deformation. Lead termination occurred when the wire lead began to detach from the solder bead on the strain gauge. During wire lead termination, the signal generally appeared with normal apparent tension values, but inverted and smaller compression values. In the amplitude domain, the signal did not have the U-shaped distribution expected from the derivation

of the models. In the frequency domain, the fundamental frequency appeared doubled while multiple harmonics were present. Additional signals were obtained during the later stages of lead termination, but no predictive models could be applied to them. The observed experimental failure modes were compared to the theoretical models. These observations were arranged into an FMEA table summarizing the failure mode, causes, effects, actions taken and potential actions to take.

5.2. Contributions

The work presented in this thesis completed the introductory steps necessary to successfully verify the laboratory setup for FMEA testing of a strain gauge, providing some examples of failure modes generated on subject strain gauges. An analysis of strain gauge technology, including bonding, soldering, and measuring circuits, was conducted. These concepts were applied to the strain gauge testing station to understand how the mechanical motion was related to the strain measured by the strain gauge. This research successfully verified the operation of the strain gauge testing station for failure mode testing of strain gauges under controlled laboratory conditions. The analysis of the testing station provided the approximate forms of the time, amplitude, and frequency domain signals, verified experimentally. Though the measured signals were smaller in amplitude than the theoretical models, failure mode testing can be conducted by comparing the measured signals to control cases. This research also analyzed two such failure modes, debonding and lead termination, by developing predictive models and verifying the theoretical approaches with experimental results.

5.3. Recommendations for future work

Although this study has verified the testing station functionally operational, some recommendations for future work have been determined based on the conclusions of this research.

Further analysis of the testing station must be conducted to understand the differences between the predictive model and the experimental results. Suggested work includes replacing the current beam with a more ideal aluminum beam and testing beams of different materials. Using a beam with material properties similar to the properties of the wire of the strain gauge may account for some differences caused by the bonding agent. The loudspeaker operation and motion should also be investigated. A more accurate means of measuring displacement should also be used for the testing station.

Some potential failure modes were introduced in Chapter 4. Further work is required to produce these failure modes in the laboratory and understand all of their causes and effects. Further analysis of debonding and lead termination may also be conducted. The signals from the later stages of lead termination were unable to be modeled in this literature. Long term observation may show some other failure modes, not mentioned in this literature. Obtaining strain gauges of different grid alignments from Vishay® can provide some failure characteristics. Once further testing has been conducted on failure modes, the results must be applied to the FMEA analysis documents to provide a quick source for understanding the causes and effects of the failure modes.

This literature investigated strain gauge failure modes for the purpose of applying the results to HCF analysis on turbine engine blades. This research focused on measurements from an individual strain gauge. Strain gauges, in practice, are arranged in patterns of potentially hundreds of gauges bonded to the surface of turbine blades. Working together, these strain gauges report the status of the component under examination. This stress analysis is essential to understanding the fatigue characteristics of the blade. Further work must be conducted to understand how the failure of a single gauge or many gauges can contribute to the system as a whole.

LIST OF REFERENCES

LIST OF REFERENCES

[1] OMEGA, "The Strain Gauge," *omega.com*, [Online]. Available: http://www.omega.com/literature/transactions/volume3/strain.html [Accessed: September 24, 2006].

[2] Sensor Land, "A brief history of strain gauges," *sensorland.com*, [Online]. Available: http://www.sensorland.com/HistPage003.html [Accessed: September 4, 2006].

[3] Test Devices Inc., "High Cycle Fatigue Failure Prevention," *testdevices.com*, [Online]. Available: http://www.testdevices.com/hcf_white.htm [Accessed: April 5, 2007].

[4] Z Mazur Z et al., "Steam turbine blade failure analysis," Engineering Failure Analysis (2007), [Online]. Available: ScienceDirect, http://www.sciencedirect.com. doi:10.1016/j.engfailanal.2006.11.018.

[5] L.M. Smith, "Noise Detection Algorithms for Turbine Engine Assessments," University of Tennessee Space Institute, Tullahoma, Tennessee, 2005.

[6] K.L. Nichol, "Assessment of Current Turbine Engine High Cycle Fatigue Test Methods," *Transactions of the ASME: Journal of Engineering for Gas Turbines and Power*, vol. 125, issue 3, p. 760+, July 2003. [Online]. Available: IEEE Xplore, http://ieeexplore.ieee.org/. doi: 10.1115/1.1423913.

[7] K. Brun, "Diagnostic Methods To Detect and Avoid High-Cycle Fatigue Damage," Southwest Research Institute, [Online]. Available: http://www.swri.edu/4org/d18/mechflu/planteng/gasturb/audit.htm [Accessed: April 4, 2007].

[8] J. Szwedowicz, S.M. Senn, and R.S. Abhari, "Optimum Strain Gauge Placement to Bladed Assemblies," *Transactions of the ASME: Journal of Turbomachinery*, vol. 124, p. 606+, October 2002. [Online]. Available: IEEE Xplore, http://ieeexplore.ieee.org/. doi: 10.1115/1.1506957.

[9] New Product Development Solutions, "Failure Modes and Effect Analysis," *npd-solutions.com*, [Online]. Available: http://www.npd-solutions.com/fmea.html [Accessed: April 5, 2007].

[10] National Instruments, “Measuring Strain with Strain Gauges,” *ni.com*, [Online]. Available: http://zone.ni.com/devzone/cda/tut/p/id/3642 [Accessed: September 14, 2006].

[11] Foley, R., “Stress, Strain, and Hooke’s Law,” *physics.uwstout.edu*, [Online]. Available: http://physics.uwstout.edu/StatStr/statics/Stress/strs31.htm [Accessed: March 12, 2007].

[12] eFunda: Engineering Fundamentals, “Electric Resistance Strain Gages,” *efunda.com*, [Online]. Available: http://www.efunda.com/designstandards/sensors/strain_gages/ [Accessed: February 10, 2007].

[13] Vishay Micro-measurements®, Tech Note TN-505-4, pp. 1-4.

[14] J.W. Dally, W.F. Riley, and K.G. McConnell, *Instrumentation for Engineering Measurements*, 2nd ed. New York: Wiley, 1993, pp 212-214.

[15] Vishay Micro-measurements®, Tech Note TN-508.

[16] “Strain Gauge Specifications,” *globalspec.com*, [Online]. Available: http://test-equipment.globalspec.com/Specifications/Test_Measurement/Product_Material_Testing/Strain_Gauges [Accessed March 2, 2007].

[17] eFunda: Engineering Fundamentals, “Poisson’s Ratio from Uniaxial Tension,” *efunda.com*, [Online]. Available: http://www.efunda.com/formulae/solid_mechanics/mat_mechanics/elastic_constants_E_nu.cfm [Accessed: February 10, 2007].

[18] All About Circuits, “Strain gauges,” *allaboutcircuits.com*, [Online]. Available: http://www.allaboutcircuits.com/vol_1/chpt_9/7.html [Accessed: August 20, 2006].

[19] Vishay Micro-measurements®, “General Purpose Strain Gages – Linear Pattern,” Data Sheet, 062AP, Document Number: 11079.

[20] eFunda: Engineering Fundamentals, “Strain Gage Wire Material Selections,” *efunda.com*, [Online]. Available: http://www.efunda.com/designstandards/sensors/strain_gages/strain_gage_sensitivity.cfm [Accessed: February 28, 2007].

[21] Vishay Micro-measurements®, “Strain Gage Installations with M-Bond 200 Adhesive,” Instruction Bulletin B-127-14.

[22] Vishay Micro-measurements®, “Soldering Techniques for Lead Attachment to Strain Gages with Solder Dots,” Tech Tip TT-606.

[23] Vishay Micro-measurements®, “Strain Gage Soldering Techniques”, Tech Tip TT-609.

[24] A. Ottenheimer, “PHPlot – Summary,” [Online]. Available: http://www.jeo.net/php/phplot/ [Accessed: December 2, 2005].

[25] eFunda: Engineering Fundamentals, “Euler-Bernoulli Beam Equation,” *efunda.com*, [Online]. Available: http://www.efunda.com/formulae/solid_mechanics/beams/theory.cfm [Accessed: March 28, 2007].

[26] Design Build Network, “Cantilever”, *designbuild-network.com*, [Online]. Available: http://www.designbuild-network.com/glossary/cantilever.html [Accessed: January 27, 2007].

[27] W.C. Young and R.G. Budynas, *Roark’s Formulas for Stress and Strain*, 7th ed. New York: McGraw Hill, 2002, p. 189.

[28] The Geometry Center, “Modeling Deflections in Beams,” *geom.uiuc.edu*, [Online]. Available: http://www.geom.uiuc.edu/education/calc-init/static-beam/modeling.html [Accessed: February 3, 2007].

[29] W.C. Young and R.G. Budynas, *Roark’s Formulas for Stress and Strain*, 7th ed. New York: McGraw Hill, 2002.

[30] National Instruments, “Stress and Strain,” *ni.com*, [Online]. Available: http://zone.ni.com/devzone/cda/ph/p/id/250 [Accessed January 25, 2007].

[31] Answers.com, “Definition of Frequency,” *answers.com*, [Online]. Available: http://www.answers.com/frequency [Accessed: October, 23, 2006].

[32] Answers.com, “Definition of Histogram,” *answers.com*, [Online]. Available: http://www.answers.com/topic/histogram [Accessed: October, 23, 2006].

[33] L.M. Smith and B. Bomar, “Spectral analysis of signals using the DFT,” Short Course at the University of Tennessee Space Institute, 2006.

[34] Interface: Advanced Force Measurement, “Load Cell Fatigue Failure Modes,” *interfaceforce.com*, [Online]. Available: http://www.interfaceforce.com/supporttheory/fatigue_modes.htm [Accessed: April 2, 2007].

[35] L. Shull, “Reliable Strain Gauge Installation,” *ERI Newsletter*, February 2002, vol. 6, [Online]. Available: http://www.vibrationandshock.com/news/news6/nl6.htm [Accessed: April 4, 2007].

[36] Vishay Micro-measurements®, “Strain Gauge Knowledge Base”, *vishay.com*, [Online]. Available: http://www.vishay.com/ [Accessed: October 20, 2005].

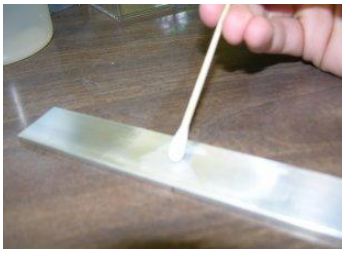
[37] International Concrete Repair Institute, “Concrete Repair Terminology,” *icri.org*, [Online]. Available: http://www.icri.org/GENERAL/ConcreteRepairTerminology.pdf [Accessed: April 4, 2007].

[38] C.A. Corral, “Combining standard component values improves circuit designs,” *Electronics Design Strategy, News*, July 7, 2001. [Online]. Available: http://www.edn.com/article/CA90755.html?1=1 [Accessed: April 2, 2007].

APPENDICES

APPENDIX A

Proper Bonding Procedures

Steps, Descriptions, and Materials	Images
Step 1: Degreasing the Surface Degrease surface using isopropyl alcohol. Wipe dry with one gauze sponge in a single direction. **Materials:** Bonding Surface, GC-6 Isopropyl Alcohol, GSP-1 Gauze Sponge	 **Figure 43: Bonding step 1**
Step 2: Dry Abrasion Dry abrade the surface with the silicon-carbide paper. Wipe away excess with one gauze sponge. **Materials:** Bonding Surface, SCP-3 Silicon-Carbide Paper, 400 Grit, GSP-1 Gauze Sponge	 **Figure 44: Bonding step 2**
Step 3: Wet Abrasion Wet abrade with M-PREP Conditioner A and the silicon-carbide paper. Wipe dry with one gauze sponge in a single direction. **Materials:** Bonding Surface, SCP-3 Silicon-Carbide Paper, 400 Grit, MCA-2 M-PREP Conditioner 5A, GSP-1 Gauze Sponge	 **Figure 45: Bonding step 3**
Step 4: Neutralizing Apply small amount of M-PREP Neutralizer A with cotton swab. Wipe dry with one gauze sponge in a single direction. **Materials:** Bonding Surface, MN5A-2 M-PREP Neutralizer 5A, CSP-1 Cotton Swabs, GSP-1 Gauze Sponges	 **Figure 46: Bonding step 4**

Step 5: Bonding Surface
The bonding surface is now prepared for the strain gauge to be connected.



Figure 47: Bonding step 5

Step 6: Preparing the Strain Gauge
Remove the strain gauge from its pouch and place bonding side down on a clean surface. Apply a piece of tape to the top side of the gauge.
Materials: EA-06-062AP-120 Strain Gauges, PCT-2M Gage Installation Tape



Figure 48: Bonding step 6

Step 7: Positioning the Strain Gauge
Apply the strain gauge to the bonding surface. For this research, the strain gauge is positioned 25 mm from square block.
Materials: Bonding Surface, EA-06-062AP-120 Strain Gauges, PCT-2M Gage Installation Tape

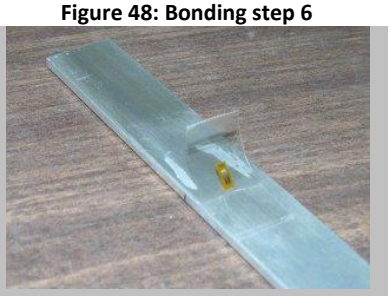


Figure 49: Bonding step 7

Step 8: Apply the Catalyst
Apply M-BOND 200 catalyst to back of strain gauge and let dry for about a minute.
Materials: Bonding Surface, EA-06-062AP-120 Strain Gauge, MBOND Catalyst



Figure 50: Bonding step 8

Step 9: Bonding the Strain Gauge
These steps must be applied quickly in order for optimal stain gauge mounting. Apply one or two drops of MBOND200 adhesive to the mounting surface, quickly fold down tape containing strain gauge.
Materials: Bonding Surface, MBOND Bonding Solution, EA-06-062AP-120 Strain Gauge



Figure 51: Bonding step 9

Step 10: Securing the Bond
Hold with thumb for about two minutes. The heat from a finger assists in the bonding.
Materials: Bonding Surface, Thumb



Figure 52: Bonding step 10

Step 11: Remove Tape
Slowly peel back tape leaving strain gauge attached to the mounting surface
Materials: Bonding Surface



Figure 53: Bonding step 11

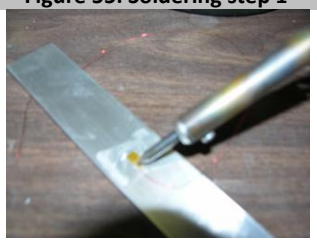
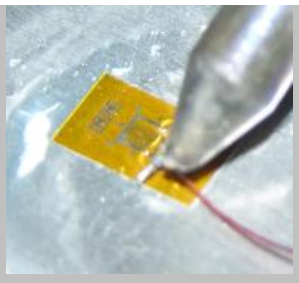
Step 12: Successful Bonding!
The gauge has been successfully bonded and leads may now be soldered onto the solder tabs.
Materials: Bonding Surface, EA-06-062AP-120 Strain Gauge



Figure 54: Bonding step 12

APPENDIX B

Proper soldering procedures

Steps, Descriptions, and Materials	Images
Step 1: Apply flux to gauge and solder Apply a large amount of flux to the strain gauge solder tabs and to the solder. **Materials:** Strain Gauge, FAR-1: M-Flux	 **Figure 55: Soldering step 1**
Step 2: Apply a solder bead to strain gauge Gather some solder on the tip of the soldering iron, and apply small bead to solder tab of the strain gauge. A sufficient amount of flux should make a better connection. **Materials:** Strain Gauge, FAR-1: M-Flux, Soldering Iron	 **Figure 56: Soldering step 2**
Step 3: Push wire into solder bead Take one end of the wire and place near solder bead. Move soldering iron close enough to melt solder bead around wire. **Materials:** Strain Gauge, Wire lead, Soldering Iron	 **Figure 57: Soldering step 3**
Step 4: Neutralize with solder rosin Apply small amount of solder rosin to neutralize the remaining flux on the strain gauge. **Materials:** Strain Gauge, FAR-1 M-Flux Rosin	 **Figure 58: Soldering step 4**

APPENDIX C

Signal conditioning circuit

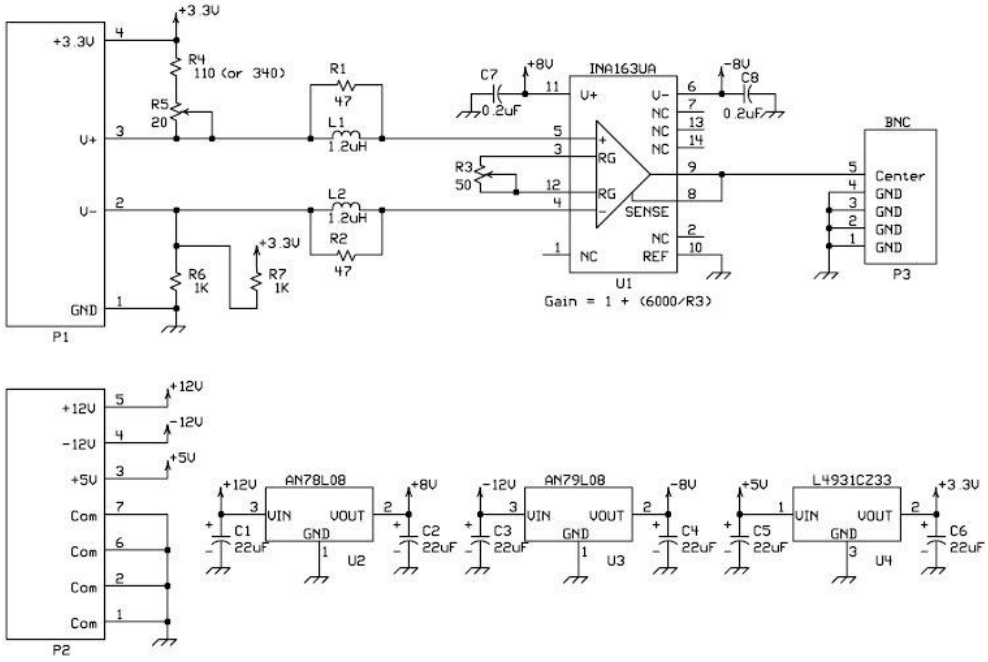


Figure 59: Signal conditioning circuit diagram

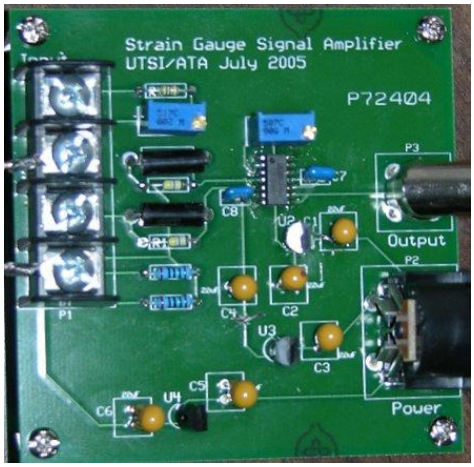
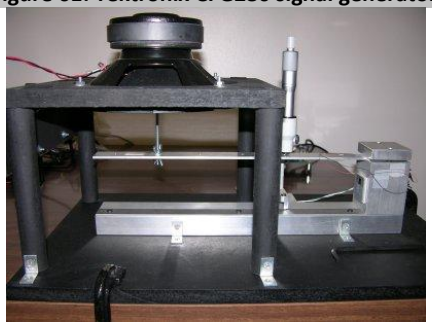


Figure 60: The signal conditioning circuit board

The signal conditioning circuit was designed and built by UTSI's Dr. Bruce Bomar.

APPENDIX D

Strain gauge testing station flow chart

Description	Figure D.1 through D.5
Tektronix CFG280 signal generator set at a particular amplitude and frequency. One output goes to the audio power amplifier, the other output goes to the digital oscilloscope.	
	Figure 61: Tektronix CFG280 signal generator
Audio power amplifier and Pioneer B20FU20-54F loudspeaker generate vertical motion on a beam. The strain gauge is mounted on the beam. A caliper measures the vertical displacement at a point 100 mm from the aluminum block. Wire leads run from strain gauge to signal conditioning circuit.	
	Figure 62: Electro-mechanical driving system
Signal conditioning circuit, consisting of a quarter-circuit Wheatstone bridge and amplifier. Output voltage sent to digital oscilloscope.	
	Figure 63: Signal conditioning circuit

Digital oscilloscope, receives input from signal generator and signal conditioning circuit.



Figure 64: Digital oscilloscope

Computer. The data from the oscilloscope is displayed by the Velleman software. Results are saved as 4096 data point ASCII text files and uploaded into the data analysis software.

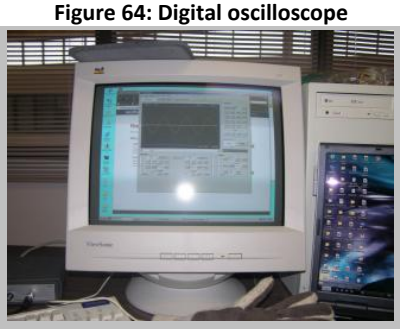


Figure 65: Computer

APPENDIX E

Amplitude domain and frequency domain (FFT) algorithms

PHP Syntax - $ indicates a variable

Amplitude domain

First determine the maximum value, $max, of the set of data, $x[$i], and define a new array, $arr, of length at least $max. Code by Dr. L. Montgomery Smith. Adapted by Brent Ellis.

```
$a = array();

$arr = array_pad($a, $max+1, 0);

for($i = 0 ; $i < 4096; $i++){

$value = $x[$i]; // determine the value of the data at index $i
$arr[$value]++; // increment the proper index by 1

}
```

Frequency domain

Calculate twiddle factors, perform FFT analysis, bit reverse, and determine magnitudes. Code by Dr. L. Montgomery Smith. Adapted by Brent Ellis.

```
// Determine twiddle factors

for($j = 0 ; $j < $N_size/2 ; $j++){

$arg = $j * $theta;
$W_Re[$j] = cos($arg);
$W_Im[$j] = sin($arg);

}

// Determine m where 2^m=N_size
$m = (log($N_size))/(log(10))/(log(2)/(log(10)));

// Perform FFT
$N = $N_size;
```

```
$N2 = $N_size;
for( $k = 0 ; $k < $m ; $k++ ){

$N1 = $N2;
$N2 /= 2;
$ie = $N / $N1;
$ia = 0;
for( $j = 0 ; $j < $N2 ; $j++ ){

$co = $W_Re[$ia];
$si = -$W_Im[$ia];
$ia += $ie;
for( $i = $j ; $i < $N ; $i += $N1 ){

$ip = $i + $N2;
$temp_Re = $x_Re[$i] - $x_Re[$ip];
$temp_Im = $x_Im[$i] - $x_Im[$ip];
$x_Re[$i] = $x_Re[$i] + $x_Re[$ip];
$x_Im[$i] = $x_Im[$i] + $x_Im[$ip];
$x_Re[$ip] = $co * $temp_Re - $si * $temp_Im;
$x_Im[$ip] = $co * $temp_Im + $si * $temp_Re;

                    }

                }

        }

// Perform bit reversal
$N1 = $N - 1;
$j = 0;
for( $i = 0 ; $i < $N1 ; $i++ ){

        if( $i < $j ){

$temp_Re = $x_Re[$j];
$temp_Im = $x_Im[$j];
$x_Re[$j] = $x_Re[$i];
$x_Im[$j] = $x_Im[$i];
$x_Re[$i] = $temp_Re;
$x_Im[$i] = $temp_Im;

        }

        $k = $N/2;
```

```
            while( $k <= $j ) {

$j -= $k;
$k /= 2;

}
$j += $k;

}

// Determine magnitude
for($j = $start; $j+1 <= $stop-1 ; $j++){

$val = SQRT($x_Re[$j]*$x_Re[$j]+$x_Im[$j]*$x_Im[$j]);
if($j == 0) $val = 0;
$pdata[] = array("", round($j * 1.5259,2) ,$val);

}
```

VITA

Brent Ellis was born on February 14th, 1983 in Memphis, Tennessee. He received his Bachelor's of Science degree in Electrical and Computer Engineering from Christian Brothers University in May of 2005. Following graduation, he attended the University of Tennessee Space Institute from 2005 to 2007, majoring in Electrical Engineering. He was married to Dr. Ashley Wimberly Ellis on December 16th, 2006 and they currently reside in Northern Virginia.